

Three-dimensional organization of promyelocytic leukemia nuclear bodies

Marion Lang^{1,2,*}, Thibaud Jegou^{2,3,*}, Inn Chung^{2,3}, Karsten Richter⁴, Sandra Münch⁵, Anikó Udvarhelyi^{2,3}, Christoph Cremer^{2,6}, Peter Hemmerich⁵, Johann Engelhardt^{1,2,†}, Stefan W. Hell^{1,2,7} and Karsten Rippe^{2,3,‡}

¹Division of High Resolution Optical Microscopy, Deutsches Krebsforschungszentrum, 69120 Heidelberg, Germany

²BioQuant, Im Neuenheimer Feld 267, 69120 Heidelberg, Germany

³Research Group Genome Organization and Function, and ⁴Division of Molecular Genetics, Deutsches Krebsforschungszentrum, 69120 Heidelberg, Germany

⁵Leibniz-Institute of Age-Research, Fritz-Lipman-Institute, 07745 Jena, Germany

⁶Applied Optics & Information Processing, Kirchhoff Institute of Physics, University of Heidelberg, 69120 Heidelberg, Germany

⁷Max Planck Institute for Biophysical Chemistry, Department of NanoBiophotonics, 37077 Göttingen, Germany

*These authors contributed equally to this paper

†Authors for correspondence (Johann.Engelhardt@dkfz.de; Karsten.Rippe@dkfz.de)

Accepted 28 October 2009

Journal of Cell Science 123, 392-400 Published by The Company of Biologists 2010

doi:10.1242/jcs.053496

Summary

Promyelocytic leukemia nuclear bodies (PML-NBs) are mobile subnuclear organelles formed by PML and Sp100 protein. They have been reported to have a role in transcription, DNA replication and repair, telomere lengthening, cell cycle control and tumor suppression. We have conducted high-resolution 4Pi fluorescence laser-scanning microscopy studies complemented with correlative electron microscopy and investigations of the accessibility of the PML-NB subcompartment. During interphase PML-NBs adopt a spherical organization characterized by the assembly of PML and Sp100 proteins into patches within a 50- to 100-nm-thick shell. This spherical shell of PML and Sp100 imposes little constraint to the exchange of components between the PML-NB interior and the nucleoplasm. Post-translational SUMO modifications, telomere repeats and heterochromatin protein 1 were found to localize in characteristic patterns with respect to PML and Sp100. From our findings, we derived a model that explains how the three-dimensional organization of PML-NBs serves to concentrate different biological activities while allowing for an efficient exchange of components.

Key words: 4Pi microscopy, Promyelocytic leukemia nuclear bodies, Sumoylation

Introduction

PML (promyelocytic leukemia) nuclear bodies (PML-NBs), also referred to as PML oncogenic domain (POD), Nuclear domain-10 (ND10) or Kremer (Kr) bodies, are mobile organelles that form distinct subcompartments in the cell nucleus as described in detail in a number of reviews (Bernardi and Pandolfi, 2007; Borden, 2008; Dellaire and Bazett-Jones, 2004; Melnick and Licht, 1999; Salomoni et al., 2008; Takahashi et al., 2004). PML-NBs appear as globular structures, 0.25 to 1 µm in diameter, in microscopy images. Typically, 5-30 PML bodies are found in a single cell, but their size and number can vary. About 80 proteins have been reported to colocalize with PML protein, as reviewed previously (Bernardi and Pandolfi, 2007; Borden, 2008; Dellaire and Bazett-Jones, 2004; Melnick and Licht, 1999; Salomoni et al., 2008; Takahashi et al., 2004). Among them are Sp100, the small ubiquitin-related modifier (SUMO), CBP (CREB-binding protein), Daxx, the Bloom's syndrome gene product (BLM) and NDP55. According to the colocalizing proteins, numerous diverse biological activities have been assigned to PML-NBs. These include transcription, antiviral defense, DNA replication and repair, telomere lengthening, chromatin organization and cell cycle control, as well as senescence, apoptosis and tumor suppression. PML protein is regarded as the central structural component of PML-NBs because these structures do not form in PML^{-/-} cells (Ishov et al., 1999). Considerable interest in the biological function of PML originates from its role in acute promyelocytic leukemia (APL), in which a chromosomal translocation fuses the *PML* gene on chromosome 15q22 with the retinoic acid receptor (*RAR*) gene

on chromosome 17q21 (Melnick and Licht, 1999). Furthermore, PML expression appears to be lost or reduced in many different human tumors, and PML^{-/-} mice are highly susceptible to chemically induced or spontaneous tumorigenesis, pointing to the role of PML as a tumor suppressor (Bernardi and Pandolfi, 2007; Salomoni et al., 2008).

Seven splicing variants of the PML protein have been identified, with PMLI and PMLII being the most abundant. All PML isoforms include the N-terminus, but differ in the central core domain as well as the C-terminus. The N-terminus of PML contains three cysteine-rich metal-binding motifs (Goddard et al., 1991), a RING finger and two B-boxes (Borden et al., 1996), followed by a coiled-coil domain (Kastner et al., 1992; Perez et al., 1993). These three motifs are referred to as RBCC or TRIM domains, and are important for self-association of PML protein (Kentsis et al., 2002). In addition, PML has three modification sites for SUMO at Lys65, Lys160 and Lys490 (Kamitani et al., 1998a; Lallemand-Breitenbach et al., 2001) as well as a SUMO-interacting motif (SIM) (Fu et al., 2005; Kamitani et al., 1998b; Shen et al., 2006; Song et al., 2004; Sternsdorf et al., 1997). In addition, it has been proposed that PML itself has an E3 SUMO ligase activity that is located in its RING domain (Quimby et al., 2006; Shen et al., 2006). PML-NBs are highly sumoylated at interphase, but not during the metaphase, when the PML protein is found in particles that lack most of the PML colocalization partners (Everett et al., 1999). In particular, the Sp100 protein, which is regarded as a constitutive structural component of interphase PML-NBs and itself contains a sumoylation site and a SIM (Seeler et al., 2001; Sternsdorf et al., 1999; Sternsdorf et al.,

1997), no longer associates with PML protein during metaphase. Thus, the formation of distinct PML-NBs appears to be critically dependent on: (1) the self-association properties of PML protein via its RBCC domain; (2) sumoylation in conjunction with the presence of a SIM in the PML protein; and (3) the incorporation of Sp100 into PML-NBs.

The structure of PML-NBs is usually described as ring-like or doughnut-shaped (Bernardi and Pandolfi, 2007; Dellaire and Bazett-Jones, 2004; Melnick and Licht, 1999; Salomoni and Pandolfi, 2002). This notion is based on imaging of immunostained PML protein (or colocalizing proteins) by confocal laser-scanning microscopy (CLSM) and electron microscopy (EM) (Boisvert et al., 2000a; Koken et al., 1994; Weis et al., 1994). The EM micrographs of immuno-gold-labeled PML-NBs in HeLa cells were described as 'dense black grains lying over roughly spheroid particles that often display a doughnut-like morphology with typical diameters of 0.3 to 0.5 μm ' (Weis et al., 1994). PML-NBs visualized by immunostaining of a stably transfected CHO cell line as well as primary human haematopoietic cells showed spherical structures of 0.3–1 μm in diameter, with an outer electron-dense fibrillar capsule stained by the PML antibody (Koken et al., 1994). By transmission electron microscopy and electron spectroscopic imaging (ESI) of human neuroblastoma SK-N-SH cells, PML-NBs were characterized as spherical, dense and protein-based structures of 250 nm in diameter (Boisvert et al., 2000b). The structure of PML-NBs in two human cell lines was found to be insensitive to RNase and DNase treatment (Weis et al., 1994) and devoid of nucleic acids (Boisvert et al., 2000b). In agreement with this result, the mobility of PML-NBs in HeLa cells resembled that of a bona fide inert particle, and no indication for (transient) chromatin binding was detected (Görisch et al., 2004). However, in other cell types, chromatin can be an integral part of PML-NBs. Most notably, a particular class of PML-NBs exists in tumor cells that maintain their telomeres in the absence of telomerase activity by a process referred to as alternative lengthening of telomeres (ALT) (Neumann and Reddel, 2006). In these cells, specific complexes of PML-NBs and telomeres exist, which are termed ALT-associated PML bodies (APBs) (Neumann and Reddel, 2006; Yeager et al., 1999). Furthermore, in lymphocytes of patients with immunodeficiency, centromeric instability and facial dysmorphism (ICF) syndrome, extremely large PML bodies (~3 μm in diameter) are found that are organized in several protein layers around a heterochromatin core of satellite DNA (Luciani et al., 2006).

PML-NBs seem to be functionally heterogeneous and dynamic structures. They have been associated with a remarkably large number of activities in the nucleus. In general, these are not directly related to the PML or Sp100 protein itself but to proteins that colocalize with PML-NBs. This suggests that the subcompartment formed by PML per se does not provide a specific activity but rather acts like a 'mobile toolbox' in the nucleus, in which specific nuclear activities are enriched. Thus, the question is raised how the structure of PML-NBs could provide such an assembly platform for other factors. Although PML-NBs were imaged in numerous fluorescence microscopy studies, the diffraction-limited resolution prevented a detailed elucidation of the PML-NB ultrastructure. The high-resolution electron micrographs, by contrast, lack information on the three-dimensional structure of the PML body and the distribution of its components within this domain. It is noted that the circular arrangement of PML protein observed on EM images would also be compatible with other shapes besides a doughnut or ring. These limitations of previous studies can be addressed by making use of

the recent advancements in fluorescence microscopy techniques that yield three-dimensional (3D) images with resolutions significantly better than those obtained by conventional CLSM (Hell, 2007). The first concept to substantially improve the 3D optical resolution, 4Pi microscopy (Hell and Stelzer, 1992; Hell, 2007), has already advanced beyond the stage of an experimental optical set-up. It has been applied successfully for studies of cell membrane delineation, cytoskeleton structures, mitochondria, the Golgi complex, histone H2A.X chromatin structures and nuclear pore complexes (Bewersdorf et al., 2006; Egner et al., 2002; Hüve et al., 2008; Lang et al., 2007b). In 4Pi microscopy, an axial resolution (i.e. the resolution along the z -axis) of 100 nm is achieved by using two opposing high numerical aperture objectives. The coherent superposition of the focused beams enlarges the effective solid angle of the wave front of the focused laser light and/or of the collected fluorescence. This yields a narrowed maximum of the PSF accompanied by axially shifted side lobes. These side lobes can be removed by image processing to obtain images with a five- to sevenfold improved axial resolution compared with conventional confocal microscopy (Gugel et al., 2004).

Here, PML bodies in U2OS and HeLa human cell lines were investigated with respect to their ultrastructure by 4Pi microscopy and correlative electron microscopy and their accessibility for diffusing molecules was assessed. The results demonstrate that during interphase, PML-NBs are spheres defined by a shell of PML and Sp100 proteins in distinct patches. Furthermore, the relative location of SUMO-1, SUMO-2/3, heterochromatin protein 1 (HP1) and telomeres to the PML-Sp100 spherical shell was determined. From the results of the ultrastructure analysis a model is derived that explains how various biological activities can be concentrated in PML-NBs in a dynamic manner.

Results

PML-NBs are spheres with a shell of PML and Sp100 protein in distinct patches

To elucidate the structure of the PML-NBs, we acquired images of immunostained PML protein by 4Pi microscopy and conventional CLSM (Fig. 1A,B, supplementary material Fig. S1-S3). The x - z and x - y sections of the 4Pi images with 1-photon or 2-photon excitation revealed that the PML protein formed a spherical shell of variable diameter in human U2OS and HeLa cells (Fig. 1A,B, supplementary material Fig. S2). With both types of excitation, equivalent images were obtained. Accordingly, 1-photon excitation was used in further experiments, because it provided a better signal intensity and bleaching was reduced. In contrast to the images acquired by 4Pi-microscopy, the conventional CLSM images showed a reduced fluorescence signal in the interior of PML-NBs only for the unusual large PML-NBs with a diameter above 1 μm in the x - y optical section (supplementary material Fig. S3A). The labeling of PML-NBs via autofluorescent mRFP1-PML-III yielded the same distribution of PML protein in a spherical shell as in the immunostaining experiments (supplementary material Fig. S2D, Fig. S3B-D). This confirmed that the antibody staining provided a faithful representation of the PML protein distribution. By two-color labeling of PML and Sp100 protein, it was apparent that Sp100 occupied the same spherical shell as PML protein in both U2OS and HeLa cells (Fig. 1C). Both proteins assembled into distinct patches with no apparent overlap whereas in some parts of the shell, PML and Sp100 colocalized. To ensure that the observed variation in PML protein density was not an artifact of the dual antibody labeling procedure, an analysis of immunostaining to PML only

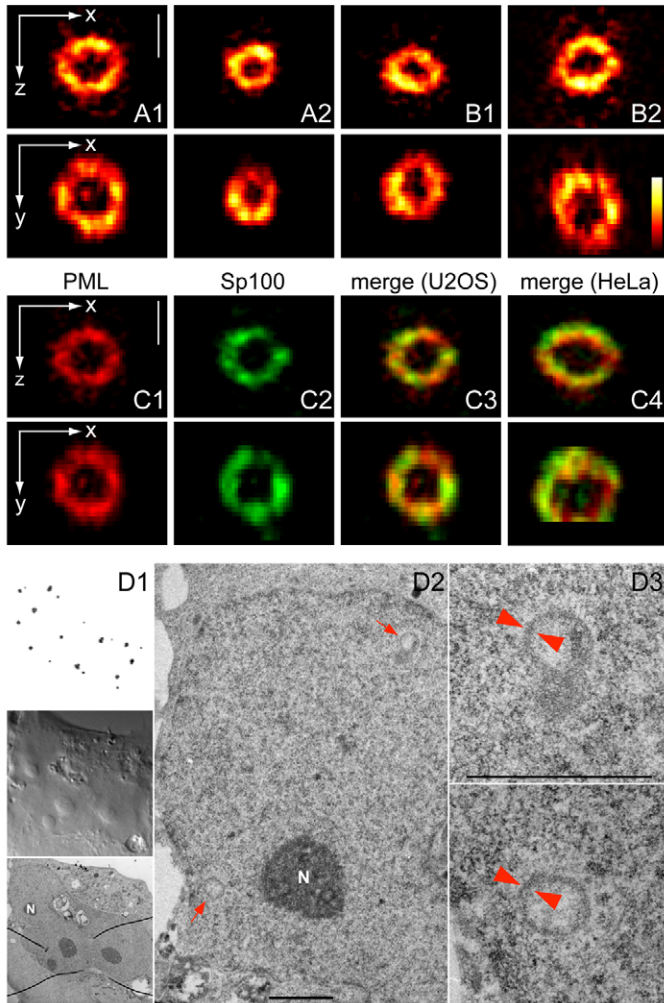


Fig. 1. 4Pi and electron microscopy of PML-NBs in U2OS and HeLa cells. (A,B) PML bodies were visualized by immunostaining with an antibody against PML and an Alexa-Fluor-568-coupled secondary antibody. The 4Pi microscopy images of x - z and x - y sections reveal that the PML protein is localized in the outer shell of a sphere of variable diameter in human U2OS (A) and HeLa cells (B). (C) Two-color 4Pi microscopy images of PML and Sp100 in a U2OS cell (C1-C3) and a HeLa cell (C4). The cells were stained with an Atto647 (PML)- and Cy3 (Sp100)-labeled secondary antibody. PML and Sp100 display only a partial colocalization in a spherical shell of identical shape. (D) Correlative fluorescence and electron microscopy of PML-NBs in U2OS cells. (D1) A nucleus of interest was chosen according to its GFP-PML autofluorescence signal observed by CLSM (top). An additional DIC image was acquired (middle), to facilitate recognition of the nucleus. The three-lobed nucleus with its four nucleoli (N) is readily recognized on the electron micrograph (bottom). The four black lines are folds in the resin section. (D2) Enlarged ultrastructural view of the left nuclear lobe. A trace back of the fluorescence signals identifies seven PML-NBs, two of which are visible on this image segment as indicated by arrows. (D3) Enlarged image of two PML bodies indicated in panel D2. Both bodies are composed of a thin shell of typical thickness of about 60 nm (distance between arrowheads) and a core of loosely spread material. The shell appears layered with convoluted material attached. Scale bars: 0.5 μ m (A-C), 1 μ m (D).

was conducted (supplementary material Fig. S3B,C), as well as a transfection of PML fusion proteins with autofluorescent mRFP1 or GFP domains (supplementary material Fig. S3D,E). With all three methods, the PML protein showed a patchy distribution with intensity variations well above the noise of the fluorescence signal (supplementary material Fig. S3B).

In PML-NBs, the spherical shell of PML and Sp100 protein has a thickness of 50-100 nm independent of the body diameter

The dimensions of the spherical shell formed by PML-Sp100 can be inferred from line scans as shown in Fig. 2A for three PML bodies from the PML-NB x - z images (insets in Fig. 2B). However, the patchwork-like distribution of the two proteins made a systematic quantification of the shell dimensions difficult. Accordingly, an evaluation was conducted by image correlation spectroscopy (ICS). In this type of analysis, the averaged correlation of pixel intensities depending on their radial distance is computed from the images (Görisch et al., 2005). The resulting curve yielded two peaks for a spherical shell (Fig. 2B). The correlation length l_c for the first peak centered around zero represents the width of the shell. For the ICS analysis conducted here, it is equivalent to the average of the full-width at half-maximum sections through the shell. The maximum of the second peak in the ICS curve yielded the mean diameter of the sphere, because pixel intensities are also correlated at this separation distance. The results from the ICS analysis are presented in a plot of the shell thickness as given by l_c versus the PML-NB diameter for PML and Sp100 protein in U2OS and HeLa cells in Fig. 2C,D. The following results were obtained: (1) No difference between PML (Fig. 2C) and Sp100 protein (Fig. 2D) or between U2OS and HeLa cells (solid vs open squares in Fig. 2C,D) was detected except for the observation that the average PML-NB diameter was somewhat smaller in HeLa cells. (2) For PML protein, a shell thickness of 126 ± 13 nm ($n=56$, 38 in U2OS, 18 in HeLa) was determined, which was independent of the body diameter between 300 and 1000 nm (Fig. 2C). (3) Sp100 had a shell thickness of $l_c = 130 \pm 13$ nm ($n=22$, 11 in U2OS, 11 in HeLa) and again no dependence on the body diameter was detected (Fig. 2D).

In our 4Pi microscopy set-up, the optical resolution, i.e. the capability to distinguish two adjacent objects labeled with the same type of fluorophore, was limited to ~ 110 nm in the axial direction. Therefore, the true wall thickness of the PML-NBs might be significantly smaller than the width of ~ 130 nm determined from the image analysis. To address this point, we compared the measured modulation depth of the line profile along the z -axis (Fig. 2E) of the 4Pi raw data (Fig. 2F), with the axial intensity profiles of calculated model images. In 4Pi microscopy, the minima between the main lobe and the side lobes quickly fill up as a structure becomes thicker than 100 nm. For thin objects, the depth of the minima is more sensitive to the shell thickness than the main lobe width. This effect is also exploited in spatially modulated illumination microscopy for measuring object dimensions below the diffraction limit (Failla et al., 2002). Thus, in 4Pi microscopy, the modulation depth of the line profile along the z -axis can be used as a measure of the object dimensions (Egner et al., 2002). Fig. 2E shows calculated axial profiles for model shells with a thickness of 50 nm, 100 nm and 150 nm, respectively, in comparison to the experimentally determined profile. These model structures with varying thickness were convolved computationally with the 4Pi-PSF that was calculated according to the vectorial theory of Richards and Wolf (Richards and Wolf, 1959). The overlay of the theoretical and experimental curves showed good agreement with a wall thickness of 100 nm (Fig. 2E). Because residual aberrations led to an additional decrease of the modulation depth of the 4Pi signal, this should be considered to be an upper estimate. Thus, it is concluded that the average shell thickness was between 50 nm and 100 nm.

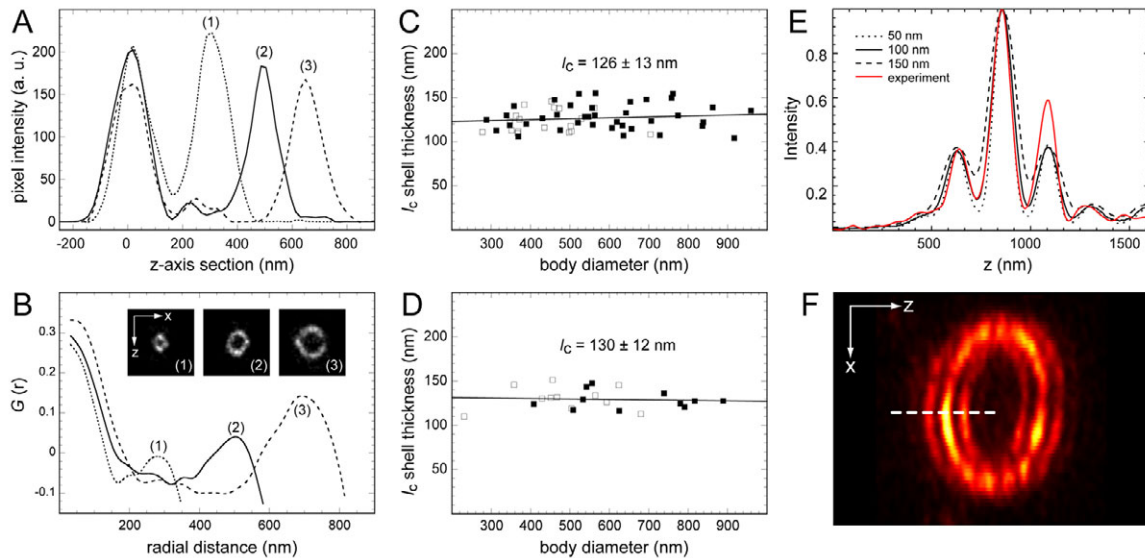


Fig. 2. Quantitative analysis of PML body structure dimensions. (A) Exemplary line profiles through PML-NBs of different diameter. (B) For a systematic analysis, the image autocorrelation function was computed and is displayed for the three PML-NBs shown in the inset. The width of the curve gives the correlation length, and from the position of the second peak the body diameter can be determined. (C) The correlation length of the PML was calculated from the autocorrelation function for PML-NBs in U2OS (solid squares) and in HeLa cells (open squares) and plotted against the corresponding body diameter. The linear regression line shows that the shell thickness as determined by the correlation length is constant at $l_c = 126 \pm 13$ nm ($n=56$, 38 in U2OS, 18 in HeLa) in the range of 300–1000 nm in diameter. The value of the correlation length corresponds to the width of the Gaussian-shaped intensity distribution at half maximum averaged over all orientations in the x - z section. (D) Sp100 in U2OS (solid squares) and in HeLa cells (open squares). The Sp100 wall thickness was $l_c = 130 \pm 13$ nm ($n=22$, 11 in U2OS, 11 in HeLa) and no dependence on the diameter is detected. (E,F) Modulation depth of the 4Pi signal. The line profile along the z -axis through a PML-NB (E) was evaluated on the 4Pi raw data depicted in F. From the modulation depth of the 4Pi line profile, the true object dimensions were estimated. Calculated intensity line profiles for shells with the same diameter as the PML-NB (i.e. $1.2 \mu\text{m}$) are shown for three different values for the wall thickness (50 nm, 100 nm, 150 nm). Good agreement with the theoretical curve for a body with ~ 100 nm shell thickness was obtained.

These results were further corroborated by electron microscopy studies. PML-NBs on electron micrographs were identified using U2OS cells transfected with autofluorescent GFP-PMLIII. Via correlation with the fluorescence signal detected beforehand on the CLSM images (Fig. 1D), PML-NBs could be identified as roughly spherical structures with a fibrillar composition. Typically, few layers of fibrillar appearance constituted a thin shell of their surface. Measured at five to eight different positions along the periphery, the median of this shell for 12 PML-NBs out of four nuclei was determined, which yielded a mean value of 56 ± 7 nm in thickness. The fibrillar pattern was modulated by globular parts, which appeared attached (supplementary material Fig. S4A,B). Although fibrillar parts could also pervade PML-NBs, their core was typically loosely occupied by convoluted material (Fig. 1D and supplementary material Fig. S4A,B). By contrast, other PML-NBs featured an accumulation of dense matter (supplementary material Fig. S4C,D). Thus, two types of PML-NBs could be distinguished with respect to their inner composition.

The PML-NB subcompartment is accessible for diffusing nuclear factors

To determine the protein mobility within PML-NBs, we performed FRAP (fluorescence recovery after photobleaching) and FCS (fluorescence correlation spectroscopy) experiments (Fig. 3). U2OS cells were co-transfected with plasmids encoding GFP tagged with a nuclear localization sequence (NLS-GFP) and mRFP1-tagged PMLIV. Confocal imaging of fixed and living cells demonstrated that the GFP fluorescence was evenly distributed throughout the nuclear volume. No difference in signal intensity was observed at

positions where PML-NBs were located. The NLS-GFP fluorescence in a rectangular region containing a PML-NB was bleached, and images were taken over several seconds. Fluorescence recovery was then quantified within the bleached region containing the PML-NB and a similarly sized region adjacent to the nuclear body. This approach revealed that the dynamics of NLS-GFP fluorescence recovery in PML-NBs and in the nucleoplasm were indistinguishable within the resolution limits of FRAP (Fig. 3). To evaluate the diffusive behavior of NLS-GFP in PML-NBs at higher spatial and temporal resolution, an FCS analysis was conducted (Fig. 3C). The FCS laser was focused into the center of a PML-NB or into the nucleoplasm. Because the confocal volume used for the FCS measurements is very close to, or even smaller than the dimensions of a PML-NB, this approach allowed us to determine the diffusion coefficient and the anomaly parameter of NLS-GFP in nuclear bodies. A threefold reduction of the diffusion coefficient inside the PML-NB was measured. In addition, the anomalous diffusion parameter α decreased from 0.93 ± 0.03 in the nucleoplasm to 0.79 ± 0.02 inside the PML-NBs. Thus, the exchange of NLS-GFP between the nucleoplasm and the PML-NB was somewhat impeded. However, the mobility of a relatively small and inert particle such as GFP was only slowed down by a factor of three, and its diffusion in and out of a PML-NBs occurred on a time scale of seconds.

SUMO-1, SUMO-2/3, HP1- β and telomere repeats occupy distinct locations in PML-NBs with respect to the PML-Sp100 protein shell

In order to determine the location of other PML-NB protein components with respect to PML and Sp100, a series of two-color

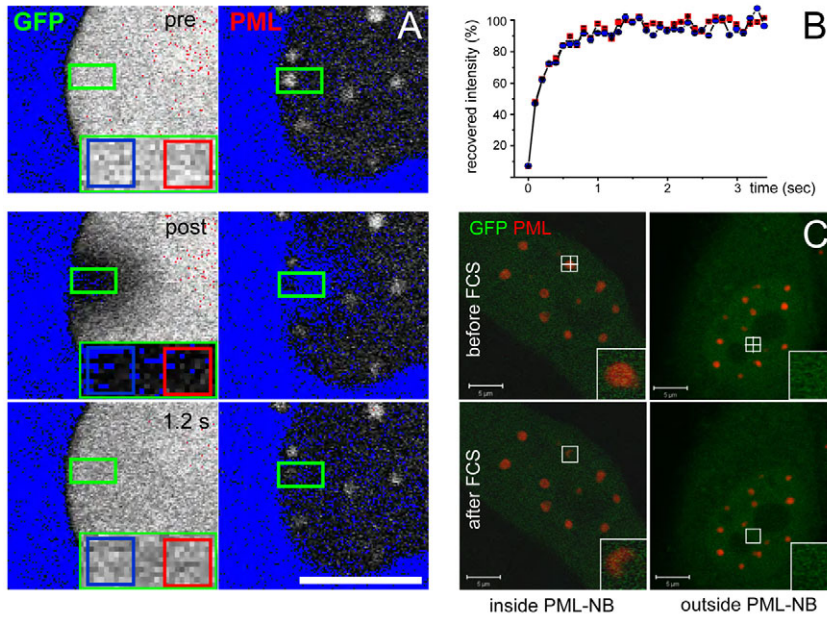


Fig. 3. Accessibility of the PML body compartment. (A) The mobility of mRFP-tagged PMLIV isoform (PML) and NLS-tagged GFP was compared in U2OS cells by FRAP to assess on which time scale the PML nuclear subcompartment was accessible. A rectangular region (in green) containing a PML-NB was bleached and images were taken before (pre), immediately after (post) and at the indicated later time points. Pixel intensities were determined over time in regions containing a nuclear body (blue rectangle) or in an adjacent, similarly sized region in the nucleoplasm (red rectangle). (B) Fluorescence intensity recovery curves (average of 10 experiments). The traces for a region with a PML-NB (blue) and without (red) are shown. (C) Accessibility of the PML body compartment probed by fluorescence correlation spectroscopy. Mid-nuclear confocal section of a HEp-2 cell co-expressing NLS-GFP and mRFP-tagged PML IV are shown before and after the FCS measurement within or outside of a PML-NB. The FCS data were fitted to an anomalous diffusion model to retrieve diffusion coefficients D and the anomalous diffusion parameter α of NLS-GFP. Values of $D=4.1\pm 0.1 \mu\text{m}^2 \text{second}^{-1}$ inside and $12.9\pm 0.4 \mu\text{m}^2 \text{second}^{-1}$ outside the PML-NB were measured. Scale bars: 5 μm .

immunostaining experiments in conjunction with 4Pi microscopy imaging was conducted (Fig. 4, supplementary material Fig. S1B). The location of SUMO modifications was investigated. The SUMO-1 protein was detected in aggregated spots in the PML-Sp100 protein shell (Fig. 4A). In general, for PML protein and SUMO-1, a partial colocalization was apparent from the line profiles. The SUMO-1 patches were less frequent and appeared more aggregated than those formed by PML protein. Interestingly, staining with an antibody that detects SUMO-2 and SUMO-3 also showed a signal in the interior in about 50% of the PML-NBs (Fig. 4B, supplementary material Fig. S5). This indicates a different distribution of SUMO paralogues in PML-NBs, with SUMO-1 being located in the PML-Sp100 shell whereas SUMO-2/3 was also present in the interior. In the other half of the investigated PML-NBs, there was only very weak SUMO-2/3 staining in the interior, and the modification was found in the shell defined by PML-Sp100-SUMO-1, as shown Fig. 4B (merge 2).

In another set of experiments, the structure of PML-NBs complexed with telomeres was investigated in U2OS cells (supplementary material Fig. S6). These so-called APBs are complexes that appear as unusually large PML-NBs on the images. They are specific for the alternative telomere-lengthening mechanism present in this cell line, and are not found in telomerase-positive cell lines such as HeLa (Jegou et al., 2009; Neumann and Reddel, 2006; Yeager et al., 1999). Under the conditions used here, about 5% of the detected telomere signals were in a complex with a PML-NB in U2OS cells, which have a total of ~ 77 chromosomes corresponding to ~ 144 telomeres (Jegou et al., 2009). For the 4Pi image analysis, the telomere repeats were stained by FISH with a Cy3-labeled (CCCTAA)₃ peptide nucleic acid probe, and PML was visualized by immunostaining. The PML protein formed a distinct shell around the telomere repeat sequence (supplementary material Fig. S6B,C). For the limited number of APBs studied here ($n=14$), the PML protein shell was between 120 nm and 140 nm as measured for regular PML-NBs.

Finally, the association of PML-NBs with heterochromatin protein 1 (HP1) was investigated, because a function of PML-NBs in heterochromatin formation via its interaction with HP1 has been

reported previously (Luciani et al., 2006). In these experiments, the PML protein was visualized by immunostaining, whereas HP1 β was detected by transient transfection with an mRFP1-HP1 β construct (supplementary material Fig. S7). The 4Pi images clearly revealed that HP1 β was located in the interior of PML-NBs. The PML shell again displayed the same apparent average thickness of ~ 130 nm ($n=11$) around the HP1 core that was measured for the other PML-NBs studied here.

During mitosis, Sp100 and SUMO-1 showed a dispersed pattern, and both proteins did not colocalize with PML particles, as was apparent on the CLSM images (supplementary material Fig. S8A). The 4Pi images of PML revealed that the spherical structure of the PML body with a distinct shell of PML and Sp100 protein had transformed into an amorphous aggregated conformation of PML multimers in metaphase (supplementary material Fig. S8B).

Discussion

PML-NB structure

In the experiments presented here, 4Pi microscopy was used to reveal details of the three-dimensional PML-NB structure that has not been reported in previous studies for any nuclear bodies. Compared with a conventional confocal microscope a five- to sevenfold improvement to about 110 nm axial resolution was achieved. Although our lateral resolution of 150–170 nm was only moderately better than that of a typical CLSM set-up (200–250 nm), a striking improvement of resolvable details in the x - y plane was apparent on the 4Pi images. The reason for this is the elongated shape of the excitation volume in z -direction of normal CLSM. This leads to a corresponding blurring of the image that obscures the resolution of structural details in the x - y plane. The results of the 4Pi imaging of PML-NBs conducted here reveal the localization of PML protein in a spherical shell. Based on an analysis of the modulation depth of the 4Pi images (Fig. 2E,F) and correlative electron microscopy studies (Fig. 1D, supplementary material Fig. S4), we determined the thickness of this shell to be around 50–100 nm. Moreover, the dimensions of this structure were found to be independent of the PML-NB diameter, as well as the specific type of PML-NB, i.e. ‘canonical’ PML-NBs, APBs or PML-NBs

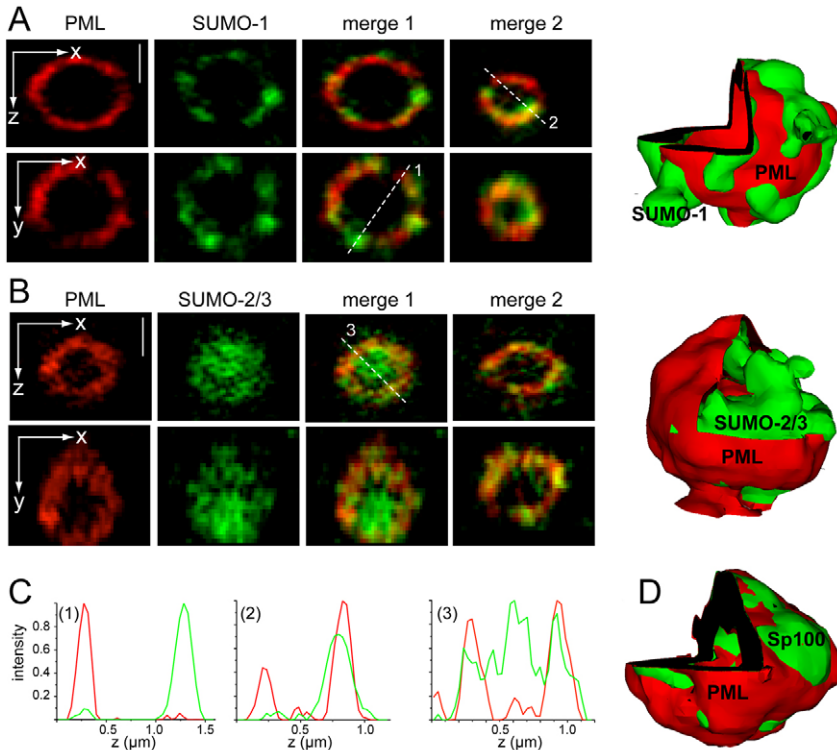


Fig. 4. Two-color 4Pi microscopy images of PML and SUMO. Immunostaining was conducted with a secondary antibody labeled with Alexa Fluor 568 (PML, red color) and Atto 647 (green color) against (A) a SUMO-1 or (B) a SUMO-2/3 primary antibody. 3D image reconstructions of the 4Pi stacks are also shown. Scale bars: 0.5 μm . The first three images show the PML, SUMO and corresponding merged image (merge 1) of one PML-NB. Then the merged PML-SUMO image of another PML-NB is presented (merge 2). SUMO-1 was distributed more sparsely and also more aggregated than PML. A partial colocalization of PML and SUMO-1 in the same spherical shell was evident from the line profiles 1 and 2. By contrast, SUMO-2/3 was located also in the interior of the PML-NB (B, merge 1). A fraction of PML-NBs showed only a very weak SUMO-2/3 signal in the interior (B, merge 2). (C) Image-intensity profiles taken along the lines indicated by numbers in A and B. (D) 3D structure of PML-Sp100 reconstructed from the images shown in Fig. 1C is shown for comparison. Sp100 was distributed similarly to PML in the outer shell of spherical shape. No extrusions from the shell were apparent but the two proteins were present in distinct patches.

containing HP1 β . This points to a self-organizing mechanism for the assembly of PML and Sp100 into a spherical shell of distinct thickness that is similar to the mechanism by which liposomes or micelles form from amphiphilic phospholipids (Kostarelos and Miller, 2005). The use of 4Pi microscopy allowed the high-resolution investigation of the two PML-NB components in the same sample. Although Sp100 was present in the same shell as PML, an enrichment of PML and Sp100 in separate regions was also apparent (Fig. 1C, Fig. 4D). The SUMO-1 protein was organized in patches that showed some intrusions and extrusions from the PML shell (Fig. 3A). This indicates that there are areas of PML protein within the shell that are strongly sumoylated, whereas little sumoylation is present in others. PML, Sp100 and SUMO-1 were confined to the outer shell part of PML-NBs. By contrast, SUMO-2/3 was found also in the interior in about 50% of the PML-NBs studied (Fig. 3B). The telomeric repeat DNA in APBs (supplementary material Fig. S6), as well as HP1 (supplementary material Fig. S7) were excluded from the PML-Sp100 shell and clearly confined to the inside of PML-NBs.

If the results obtained here are considered in the context of the large number of previous studies, several factors can be identified that determine the PML-NB structure. The N-terminal RBCC domain of PML protein has self-assembly properties, and deletions or mutations within this domain prevent PML-NB formation (Borden, 2002; Le et al., 1996). This is demonstrated by the formation of spherical structures of similar size to PML-NBs from a bacterially expressed, non-sumoylated RBCC domain (Kentsis et al., 2002). In addition, Sp100 has been reported to self-associate via its HSR domain into homodimers, which is probably also relevant for the interaction network formed between PML and Sp100 protein (Sternsdorf et al., 1999). Importantly, the structures that form via self-association of PML protein in the absence of sumoylation and Sp100 are clearly different from that of a canonical PML-NB.

This can be inferred from inspection of PML bodies in mitotic cells where the PML protein is not sumoylated and is not colocalizing with Sp100 (supplementary material Fig. S8). Under these conditions PML protein formed amorphous aggregates with a homogenous PML density throughout the particle. This is consistent with previous reports showing that sumoylation is essential for the formation of normal PML-NBs in mammalian cells (Ishov et al., 1999; Nacerddine et al., 2005; Zhong et al., 2000), and that PML-NBs are disrupted during mitosis as a result of desumoylation (Everett et al., 1999). The results from the 4Pi imaging obtained here indicate that sumoylation of PML is required for the organization of PML and Sp100 in PML-NBs in a distinct spherical shell.

The FRAP and FCS experiments demonstrate that PML-NBs are accessible for a relatively small particle such as GFP (27 kDa, cylindrically shaped with ~ 3 nm diameter and ~ 4 nm height) (Fig. 3). From inspection of the 4Pi and EM images, it appears that the PML shell is a filamentous structure, with some variations in thickness. In a recent comprehensive set of FRAP experiments, it was demonstrated that the PML protein splicing variants I-IV and VI, as well as Sp100 exchange between the PML-NB-bound state and the pool of free PML-Sp100 protein in the nucleoplasm within a time scale of seconds to minutes. By contrast, the PMLV splicing variant remained bound in the PML-NB with an average residence time of 48 minutes (Weidtkamp-Peters et al., 2008). These findings suggest that PMLV provides a stable structural scaffold for the other more mobile components of the PML-Sp100 shell. Given the relatively fast exchange of the other splicing variants I-IV and VI, it can be rationalized that the diffusion of GFP in and out of PML-NBs is only moderately slower than its mobility in the nucleoplasm. Nevertheless, the threefold reduction in diffusion rate as observed in the FCS analysis might be sufficient for an increased probability of a protein to become modified. For instance, PML bodies are

implicated as sites for both acetylation and phosphorylation of the tumor suppressor p53 (Louria-Hayon et al., 2003; Pearson et al., 2000).

The results on the PML-NB ultrastructure obtained here, together with a number of findings from previous studies, are cast into the model depicted in Fig. 5. In the absence of sumoylation, PML protein forms unspecific aggregates via the N-terminal RBCC domain of PML. Upon sumoylation of both PML and Sp100 protein, a filamentous network of PML-PML, Sp100-Sp100 and PML-Sp100 interactions is established via the SIM found in both proteins. This interaction network organizes into a spherical shell of 50-100 nm in thickness and variable diameter with patches of PML and Sp100. In the resulting PML-NB structure, SUMO-1 modifications are found preferably within the shell or adjacent to it. By contrast the SUMO-2/3 modifications were not restricted to this region, but extended into the interior for a ~50% fraction of the PML-NBs. In this context, it is noteworthy that SUMO-2/3 has the ability to form polymeric chains, because both SUMO-2 and SUMO-3 contain an internal sumoylation site that is missing in SUMO-1 (Matic et al., 2008). Because the other half of the studied bodies displayed only very little SUMO-2/3 signal in the interior, it seems that two different types of PML-NBs exist (compare merge images in Fig. 4B and supplementary material Fig. S5). This view is supported by the electron microscopy analysis, in which PML-NBs with low and high density of the material inside the PML-Sp100 shell were detected at a ratio of 1:1 (Fig. 1D, supplementary material Fig. S4). This observation might reflect the fact that PML-NBs with SUMO-2/3 in the center appear as the more densely stained bodies in the EM images. Thus, the protein composition in the interior of PML-NBs could be controlled by modulating their SUMO-2/3 content. The dynamic nature of this modification is supported by the finding that sumoylation might occur within PML-NBs (Saitoh et al., 2006) and that the presence of poly-SUMO-2/3 chains is a prerequisite for the ubiquitin-dependent degradation of PML (Lallemand-Breitenbach et al., 2008; Tatham et al., 2008). It is noted that such a mechanisms of targeted PML degradation could serve to release the SUMO-interacting proteins into the nucleoplasm so that they would exert specific activities.

Many proteins that associate with PML-NBs are sumoylated or contain a SUMO-interacting motif. This is also relevant for the complexes of PML with telomeres (supplementary material Fig. S6) and HP1 investigated here (supplementary material Fig. S7). The interaction of telomeric repeats with the PML-NBs in APBs is critically dependent on the sumoylation of telomere-binding proteins such as TRF1, TRF2, TIN2 and RAP1 by the MMS21 SUMO ligase. It was shown that APBs did not form in the absence of TRF1 or

TRF2 sumoylation (Potts and Yu, 2007). The recruitment of HP1 into PML-NBs is also related to sumoylation processes, because it has been reported that the interaction of HP1 with other proteins can be enhanced by SUMO modifications of the HP1 interaction partner (Seeler et al., 2001; Uchimura et al., 2006). Accordingly, a number of models for the PML-NB structure were proposed previously that are based on a network of SUMO-SIM interactions (Lin et al., 2006; Shen et al., 2006), albeit without the structural details on the organization of PML-NBs provided from our analysis. The clear discrimination between an inner part and an outer shell of PML-NBs obtained in this study supports the view that PML-NBs can assemble around a distinct core structure such as telomeric DNA (supplementary material Fig. S6), as shown recently in live-cell-imaging experiments (Jegou et al., 2009). The presence of a chromatin core has also been observed for the giant PML-NBs in cells from patients suffering from ICF syndrome (Luciani et al., 2006), as well as the assembly of PML-NBs around HSV-1 viral nucleoprotein complexes (Everett and Murray, 2005). Because HP1 was located in the inner part of PML-NBs (Fig. S7), it appears that the presence of HP1 could increase the propensity of a genomic locus to serve as the nucleation site for PML-NB assembly. In agreement with this view, ICF-associated PML-NBs or APBs form at heterochromatic loci such as telomeres or microsatellite DNA enriched in HP1 (Luciani et al., 2006; Yeager et al., 1999). This might contribute to the creation of a distinct nuclear subcompartment to confine associated activities to these sites.

We conclude that the ultrastructure of PML-NBs revealed here reflects the self-organizing properties of PML and Sp100 proteins in the environment of the nucleus, which are steered by sumoylation and the interaction with SIMs present in both proteins. In this context, it is also noteworthy that the SUMO modification of Sp100 is significantly decreased in the absence of PML (Everett et al., 2006). Thus, the PML-Sp100-SUMO interaction network could be established and maintained in PML-NBs in a feedback-loop manner in the presence of desumoylation activities outside this nuclear subcompartment. Such a mechanism would be further enhanced by the putative SUMO ligase activity of PML (Quimby et al., 2006; Shen et al., 2006). The resulting PML-Sp100 shell structure appears conceptually similar to the organization of a liposome. It is dynamic and allows for an exchange of proteins in and out of the PML-Sp100 shell on the second-to-minute time scale, as inferred from our studies of GFP mobility. Via a protein interaction network that makes use of SUMO-mediated binding to the SIMs of the various 'cargo' proteins, specific biological activities can be concentrated in the PML-NB subcompartment. This process could serve to promote modifications of nuclear components that require a high

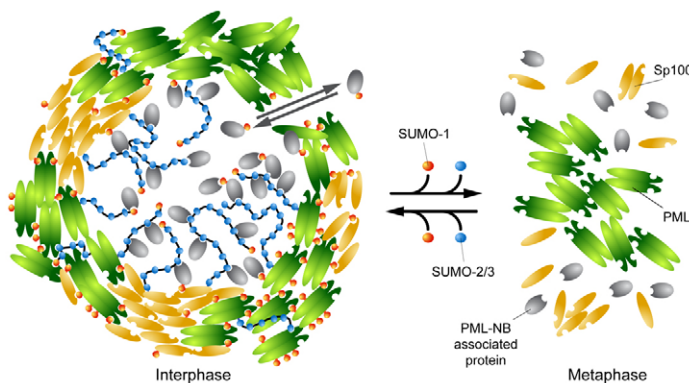


Fig. 5. Model for the structure of PML-NBs. PML proteins associate via their RBCC domains and can be covalently modified by SUMO-1, SUMO-2 and SUMO-3. The PML-NB is defined by a spherical shell stabilized via non-covalent SUMO-SIM interactions between PML and Sp100. Proteins can pass through this shell with only a moderate reduction of their diffusive mobility. The poly-SUMO-2/3 chains protrude to variable degrees into the interior of the PML-NB. These are likely to represent binding sites for SIMs of other proteins so that these are enriched in the interior of the PML-NB. Upon desumoylation during mitosis, the spherical shell structure of the PML-NBs breaks down, and only the unspecific aggregation of PML protein via its RBCC domains is retained.

concentration of these factors not available in their freely mobile state in the nucleoplasm. Alternatively, PML-NBs could represent sites of storage or confinement for certain nuclear factors that would exert their biological function only upon release from the PML-NB by removal of SUMO residues.

Materials and Methods

Cell culture and sample preparation

Human cell lines HeLa (REF) and U2OS (HTB-96) were grown in DMEM (Invitrogen) containing 10% FCS (PAA, Austria). Immunostaining and PNA FISH were conducted as described previously (Jegou et al., 2009). The primary antibodies against PML and SUMO-1 from Santa Cruz Biotechnology and against Sp100 from Chemicon (Millipore) were used. The anti-mouse Alexa Fluor 568 and anti-mouse/anti-rabbit Alexa Fluor 647 secondary antibody were purchased from Invitrogen and the anti-mouse and anti-rabbit Atto 647N were from ATTO-TEC (Siegen, Germany). Cells for 4Pi microscopy were grown on coverslips ~150 µm thick. After staining, the samples were embedded in a solution containing 97% (v/v) TDE (2,2'-thiodiethanol, Sigma) and 3% (v/v) phosphate buffered saline (PBS) to yield a refractive index of 1.515 (Staudt et al., 2007). This minimizes spherical aberration and minimizes the side lobes. To avoid structural changes, the buffer was replaced with the embedding medium via a dilution series (step-wise 10, 20, 40, 60, 80 and three times 97% TDE was applied for 10 minutes each). This coverslip was mounted on a second coverslip (with a quarter mirror for the phase setting of the 4Pi set-up) of equal thickness and sealed with nail polish. For standard CLSM, the coverslips were dipped briefly into H₂O, incubated for 1 minute in ethanol, then air-dried and finally mounted in Vectashield containing DAPI (Vector Laboratories). For analysis of autofluorescent mRFP1-PML-III and GFP-PML-III constructs, cells were transfected with Effectene (Qiagen, Hilden, Germany) incubated for about 17 hours with the transfection reagent before fixation, as described previously (Jegou et al., 2009). Complexes of PML and HP1β were visualized by transient transfection with an mRFP1-HP1β construct (Müller et al., 2009).

Fluorescence microscopy

4Pi microscopy imaging was conducted with a custom-made module attached to a conventional confocal microscope (TCS SP2, Leica Microsystems, Mannheim) as described in detail elsewhere (Gugel et al., 2004). The 4Pi module was equipped with two high numerical aperture oil-immersion objectives (HCX PL APO CS 100× 1.46 NA Oil, Leica Microsystems, Germany). These yield a narrow central maximum of an axial full-width at half-maximum (FWHM) of ~100 nm and low side maxima. 4Pi imaging was conducted with an Ar-Kr-Laser (one-photon excitation) or a Ti:Sapphire laser (two-photon excitation; Mai Tai, Newport-Spectra-Physics, Mountain View, CA). As described previously (Lang et al., 2007a), 4Pi microscopy with one-photon excitation yielded a higher signal intensity compared with 2-photon excitation at the cost of higher side maxima (supplementary material Fig. S2). Detection of the fluorescence emission was with avalanche photodiodes (PerkinElmer Optoelectronics, Fremont, CA). The 3D data stacks were recorded with a voxel size of 37×28×55 nm in the *x-z-y* direction. After image acquisition, the 4Pi raw data were processed to remove the side maxima. To this end, the 4Pi raw data were smoothed and a five-point deconvolution was applied (Nagorni and Hell, 2001). Subsequently, an offset of 10% was subtracted. No further deconvolution of the image was conducted. Standard confocal microscopy was performed with a Leica TCS SP2. Z-axis picture stacks with 0.3-µm spacing were acquired and were displayed as maximum intensity projection in the overview images. FRAP experiments were carried out on a Zeiss LSM 510Meta confocal microscope (Carl Zeiss, Jena, Germany) as described (Schmiedeberg et al., 2004). Five to ten images were taken before the bleach pulse and 50-200 images after bleaching of 'regions of interest'. FCS measurements were performed at 37°C on a LSM 510 Meta/ConfoCor2 system using a C-Apochromat infinity-corrected 40× 1.2 NA water objective (Carl Zeiss, Jena, Germany) as described in detail previously (Schmiedeberg et al., 2004; Weidtkamp-Peters et al., 2008; Weidtkamp-Peters et al., 2009). For the measurements, 10×30 time-series of 10 seconds each were recorded with a time resolution of 1 µsecond and then superimposed for fitting to an anomalous diffusion model in three dimensions with triplet function using the Origin Software. The diffusion coefficients and anomaly parameters were extracted from fitted curves as previously described (Weidtkamp-Peters et al., 2009). FRAP and FCS studies were conducted with the GFP-PML IV splicing variant.

Correlative electron microscopy

Cells transfected with GFP-tagged PML and grown on gridded coverslips (Cellocate, Eppendorf, Germany) were processed for correlative fluorescence and electron microscopy, as previously described (Richter et al., 2005). Briefly, cells were fixed in 4% formaldehyde, 1% glutaraldehyde (EM-grade, Sigma) in 100 mM sodium phosphate buffer, rinsed with buffer and mounted with Vectashield (Vector laboratories) for observation by confocal laser scanning microscopy (TCS-SP II, Leica Microsystems, Germany). CLSM data of cell nuclei of interest comprised 3D-image stacks of GFP-PML at 74 nm pixel size using a 100× 1.4 NA oil objective, and a differential interference contrast image to assist relocation after preparation for EM. Following CLSM investigation, the coverslips were post-fixed in 1% buffered OsO₄,

dehydrated in graded steps of ethanol and embedded in epoxy resin (Polysciences, Eppelheim, Germany). The coverslips were removed under liquid nitrogen, depicting the negative imprint of the grid on the remaining block faces. Ultrathin sections at nominal thickness of 70 nm were prepared from the grid-region of interest, stained in aqueous lead citrate and uranyl acetate and observed in a Philips 410 transmission electron microscope.

We are grateful to David Baddeley, Malte Wachsmuth and Joel Beaudoin for help and discussions. The work was funded by the Deutsche Forschungsgemeinschaft (Ri 1283/5-3) in the SPP 1128 program (K.R.) and within the project 'Neue 4Pi-Kontraste zur Abbildung lebender Zellen' of the Landesstiftung Baden-Württemberg (S.W.H.).

Supplementary material available online at

<http://jcs.biologists.org/cgi/content/full/123/3/392/DC1>

References

- Bernardi, R. and Pandolfi, P. P. (2007). Structure, dynamics and functions of promyelocytic leukaemia nuclear bodies. *Nat. Rev. Mol. Cell Biol.* **8**, 1006-1016.
- Bewersdorf, J., Bennett, B. and Knight, K. (2006). H2AX chromatin structures and their response to DNA damage revealed by 4Pi microscopy. *Proc. Natl. Acad. Sci. USA* **103**, 18137-18142.
- Boisvert, F. M., Hendzel, M. J. and Bazett-Jones, D. P. (2000a). Promyelocytic leukemia (PML) nuclear bodies are protein structures that do not accumulate RNA. *J. Cell Biol.* **148**, 283-292.
- Boisvert, F. M., Hendzel, M. J. and Bazett-Jones, D. P. (2000b). Promyelocytic leukemia (PML) nuclear bodies are protein structures that do not accumulate RNA. *J. Cell Biol.* **148**, 283-292.
- Borden, K. L. (2002). Pondering the promyelocytic leukemia protein (PML) puzzle: possible functions for PML nuclear bodies. *Mol. Cell Biol.* **22**, 5259-5269.
- Borden, K. L. (2008). Pondering the puzzle of PML (promyelocytic leukemia) nuclear bodies: can we fit the pieces together using an RNA regulon? *Biochim. Biophys. Acta* **1783**, 2145-2154.
- Borden, K. L., Lally, J. M., Martin, S. R., O'Reilly, N. J., Solomon, E. and Freemont, P. S. (1996). In vivo and in vitro characterization of the B1 and B2 zinc-binding domains from the acute promyelocytic leukemia proto-oncoprotein PML. *Proc. Natl. Acad. Sci. USA* **93**, 1601-1606.
- Dellaire, G. and Bazett-Jones, D. P. (2004). PML nuclear bodies: dynamic sensors of DNA damage and cellular stress. *BioEssays* **26**, 963-977.
- Eger, A., Jakobs, S. and Hell, S. W. (2002). Fast 100-nm resolution 3D-microscope reveals structural plasticity of mitochondria in live yeast. *Proc. Natl. Acad. Sci. USA* **99**, 3370-3375.
- Everett, R. D. and Murray, J. (2005). ND10 components relocate to sites associated with herpes simplex virus type 1 nucleoprotein complexes during virus infection. *J. Virol.* **79**, 5078-5089.
- Everett, R. D., Lomonte, P., Sternsdorf, T., van Driel, R. and Orr, A. (1999). Cell cycle regulation of PML modification and ND10 composition. *J. Cell Sci.* **112**, 4581-4588.
- Everett, R. D., Rechter, S., Papior, P., Tavalai, N., Stamminger, T. and Orr, A. (2006). PML contributes to a cellular mechanism of repression of herpes simplex virus type 1 infection that is inactivated by ICP0. *J. Virol.* **80**, 7995-8005.
- Failla, A. V., Spoeri, U., Albrecht, B., Kroll, A. and Cremer, C. (2002). Nanosizing of fluorescent objects by spatially modulated illumination microscopy. *Appl. Optics* **41**, 7275-7283.
- Fu, C., Ahmed, K., Ding, H., Ding, X., Lan, J., Yang, Z., Miao, Y., Zhu, Y., Shi, Y., Zhu, J. et al. (2005). Stabilization of PML nuclear localization by conjugation and oligomerization of SUMO-3. *Oncogene* **24**, 5401-5413.
- Goddard, A. D., Borrow, J., Freemont, P. S. and Solomon, E. (1991). Characterization of a zinc finger gene disrupted by the t(15;17) in acute promyelocytic leukemia. *Science* **254**, 1371-1374.
- Görisch, S. M., Wachsmuth, M., Ittrich, C., Bacher, C. P., Rippe, K. and Lichter, P. (2004). Nuclear body movement is determined by chromatin accessibility and dynamics. *Proc. Natl. Acad. Sci. USA* **101**, 13221-13226.
- Görisch, S. M., Wachsmuth, M., Fejes Tóth, K., Lichter, P. and Rippe, K. (2005). Histone acetylation increases chromatin accessibility. *J. Cell Sci.* **118**, 5825-5834.
- Gugel, H., Bewersdorf, J., Jakobs, S., Engelhardt, J., Storz, R. and Hell, S. W. (2004). Cooperative 4Pi excitation and detection yields 7-fold sharper optical sections in live cell microscopy. *Biophys. J.* **87**, 4146-4152.
- Hell, S. W. (2007). Far-field optical nanoscopy. *Science* **316**, 1153-1158.
- Hell, S. and Stelzer, E. H. K. (1992). Properties of a 4Pi-confocal fluorescence microscope. *J. Opt. Soc. Am. A* **9**, 2159-2166.
- Hüve, J., Wesselmann, R., Kahms, M. and Peters, R. (2008). 4Pi microscopy of the nuclear pore complex. *Biophys. J.* **95**, 877-885.
- Ishov, A. M., Sotnikov, A. G., Negorev, D., Vladimirova, O. V., Neff, N., Kamitani, T., Yeh, E. T., Strauss, J. F., 3rd and Maul, G. G. (1999). PML is critical for ND10 formation and recruits the PML-interacting protein daxx to this nuclear structure when modified by SUMO-1. *J. Cell Biol.* **147**, 221-234.
- Jegou, T., Chung, I., Heuvelmann, G., Wachsmuth, M., Görisch, S. M., Greulich-Bode, K., Boukamp, P., Lichter, P. and Rippe, K. (2009). Dynamics of telomeres and promyelocytic leukemia nuclear bodies in a telomerase negative human cell line. *Mol. Biol. Cell* **20**, 2070-2082.

- Kamitani, T., Kito, K., Nguyen, H. P., Wada, H., Fukuda-Kamitani, T. and Yeh, E. T. (1998a). Identification of three major sentrinization sites in PML. *J. Biol. Chem.* **273**, 26675-26682.
- Kamitani, T., Nguyen, H. P., Kito, K., Fukuda-Kamitani, T. and Yeh, E. T. (1998b). Covalent modification of PML by the sentrin family of ubiquitin-like proteins. *J. Biol. Chem.* **273**, 3117-3120.
- Kastner, P., Perez, A., Lutz, Y., Rochette-Egly, C., Gaub, M. P., Durand, B., Lanotte, M., Berger, R. and Chambon, P. (1992). Structure, localization and transcriptional properties of two classes of retinoic acid receptor alpha fusion proteins in acute promyelocytic leukemia (APL): structural similarities with a new family of oncoproteins. *EMBO J.* **11**, 629-642.
- Kentsis, A., Gordon, R. E. and Borden, K. L. (2002). Self-assembly properties of a model RING domain. *Proc. Natl. Acad. Sci. USA* **99**, 667-672.
- Koken, M. H., Puvion-Dutilleul, F., Guillemin, M. C., Viron, A., Linares-Cruz, G., Stuurman, N., de Jong, L., Szostecki, C., Calvo, F., Chomienne, C. et al. (1994). The t(15;17) translocation alters a nuclear body in a retinoic acid-reversible fashion. *EMBO J.* **13**, 1073-1083.
- Kostarelos, K. and Miller, A. D. (2005). Synthetic, self-assembly ABCD nanoparticles; a structural paradigm for viable synthetic non-viral vectors. *Chem. Soc. Rev.* **34**, 970-994.
- Lallemand-Breitenbach, V., Zhu, J., Puvion, F., Koken, M., Honore, N., Doubeikovsky, A., Duprez, E., Pandolfi, P. P., Puvion, E., Freemont, P. et al. (2001). Role of promyelocytic leukemia (PML) sumolation in nuclear body formation, 11S proteasome recruitment, and As2O3-induced PML or PML/retinoic acid receptor alpha degradation. *J. Exp. Med.* **193**, 1361-1371.
- Lallemand-Breitenbach, V., Jeanne, M., Benhenda, S., Nasr, R., Lei, M., Peres, L., Zhou, J., Zhu, J., Raught, B. and de The, H. (2008). Arsenic degrades PML or PML-RARalpha through a SUMO-triggered RNF4/ubiquitin-mediated pathway. *Nat. Cell Biol.* **10**, 547-555.
- Lang, M., Engelhardt, J. and Hell, S. W. (2007a). 4Pi microscopy with linear fluorescence excitation. *Opt. Lett.* **32**, 259-261.
- Lang, M., Müller, T., Engelhardt, J. and Hell, S. W. (2007b). 4Pi microscopy of type A with 1-photon excitation in biological fluorescence imaging. *Opt. Express* **15**, 2459-2467.
- Le, X. F., Yang, P. and Chang, K. S. (1996). Analysis of the growth and transformation suppressor domains of promyelocytic leukemia gene, PML. *J. Biol. Chem.* **271**, 130-135.
- Lin, D. Y., Huang, Y. S., Jeng, J. C., Kuo, H. Y., Chang, C. C., Chao, T. T., Ho, C. C., Chen, Y. C., Lin, T. P., Fang, H. I. et al. (2006). Role of SUMO-interacting motif in Daxx SUMO modification, subnuclear localization, and repression of sumoylated transcription factors. *Mol. Cell* **24**, 341-354.
- Louria-Hayon, I., Grossman, T., Sionov, R. V., Alsheich, O., Pandolfi, P. P. and Haupt, Y. (2003). The promyelocytic leukemia protein protects p53 from Mdm2-mediated inhibition and degradation. *J. Biol. Chem.* **278**, 33134-33141.
- Luciani, J. J., Depetris, D., Usson, Y., Metzler-Guillemain, C., Mignon-Ravix, C., Mitchell, M. J., Megarbane, A., Sarda, P., Sirma, H., Moncla, A. et al. (2006). PML nuclear bodies are highly organised DNA-protein structures with a function in heterochromatin remodelling at the G2 phase. *J. Cell Sci.* **119**, 2518-2531.
- Matic, I., van Hagen, M., Schimmel, J., Macek, B., Ogg, S. C., Tatham, M. H., Hay, R. T., Lamond, A. I., Mann, M. and Vertegaal, A. C. (2008). In vivo identification of human small ubiquitin-like modifier polymerization sites by high accuracy mass spectrometry and an in vitro to in vivo strategy. *Mol. Cell Proteomics* **7**, 132-144.
- Melnick, A. and Licht, J. D. (1999). Deconstructing a disease: RARalpha, its fusion partners, and their roles in the pathogenesis of acute promyelocytic leukemia. *Blood* **93**, 3167-3215.
- Müller, K., Erdel, F., Caudron-Herger, M., Marth, C., Fodor, B. D., Richter, M., Scaranaro, M., Beoudoin, J., Wachsmuth, M. and Rippe, K. (2009). A multi-scale analysis of dynamics and interactions of heterochromatin protein 1 in the nucleus by fluorescence fluctuation microscopy. *Biophys. J.* **97**, 2876-2885.
- Nacerdine, K., Lehenbre, F., Bhaumik, M., Artus, J., Cohen-Tannoudji, M., Babinet, C., Pandolfi, P. P. and Dejean, A. (2005). The SUMO pathway is essential for nuclear integrity and chromosome segregation in mice. *Dev. Cell* **9**, 769-779.
- Nagorni, M. and Hell, S. W. (2001). Coherent use of opposing lenses for axial resolution increase in fluorescence microscopy. II. Power and limitation of nonlinear image restoration. *J. Opt. Soc. Am. A* **18**, 49-54.
- Neumann, A. A. and Reddel, R. R. (2006). Telomerase-independent maintenance of mammalian telomeres. In *Telomeres* (eds T. de Lange, V. Lundblad and E. Blackburn), pp. 163-198. Cold Spring Harbor: Cold Spring Harbor Laboratory Press.
- Pearson, M., Carbone, R., Sebastiani, C., Cioco, M., Fagioli, M., Saito, S., Higashimoto, Y., Appella, E., Minucci, S., Pandolfi, P. P. et al. (2000). PML regulates p53 acetylation and premature senescence induced by oncogenic Ras. *Nature* **406**, 207-210.
- Perez, A., Kastner, P., Sethi, S., Lutz, Y., Reibel, C. and Chambon, P. (1993). PMLRAR homodimers: distinct DNA binding properties and heteromeric interactions with RXR. *EMBO J.* **12**, 3171-3182.
- Potts, P. R. and Yu, H. (2007). The SMC5/6 complex maintains telomere length in ALT cancer cells through SUMOylation of telomere-binding proteins. *Nat. Struct. Mol. Biol.* **14**, 581-590.
- Quimby, B. B., Yong-Gonzalez, V., Anan, T., Strunnikov, A. V. and Dasso, M. (2006). The promyelocytic leukemia protein stimulates SUMO conjugation in yeast. *Oncogene* **25**, 2999-3005.
- Richards, B. and Wolf, E. (1959). Electromagnetic diffraction in optical systems II. Structure of the image field in an aplanatic system. *Proc. R. Soc. Lond. A* **253**, 358-379.
- Richter, K., Reichenzeller, M., Gorisch, S. M., Schmidt, U., Scheuermann, M. O., Herrmann, H. and Lichter, P. (2005). Characterization of a nuclear compartment shared by nuclear bodies applying ectopic protein expression and correlative light and electron microscopy. *Exp. Cell Res.* **303**, 128-137.
- Saitoh, N., Uchimura, Y., Tachibana, T., Sugahara, S., Saitoh, H. and Nakao, M. (2006). In situ SUMOylation analysis reveals a modulatory role of RanBP2 in the nuclear rim and PML bodies. *Exp. Cell Res.* **312**, 1418-1430.
- Salomoni, P. and Pandolfi, P. P. (2002). The role of PML in tumor suppression. *Cell* **108**, 165-170.
- Salomoni, P., Ferguson, B. J., Wylie, A. H. and Rich, T. (2008). New insights into the role of PML in tumour suppression. *Cell Res.* **18**, 622-640.
- Schmiedeberg, L., Weisshart, K., Diekmann, S., Meyer zu Hoerste, G. and Hemmerich, P. (2004). High- and low-mobility populations of HP1 in heterochromatin of mammalian cells. *Mol. Biol. Cell* **15**, 2819-2833.
- Seeler, J. S., Marchio, A., Losson, R., Desterro, J. M., Hay, R. T., Chambon, P. and Dejean, A. (2001). Common properties of nuclear body protein SP100 and TIF1alpha chromatin factor: role of SUMO modification. *Mol. Cell Biol.* **21**, 3314-3324.
- Shen, T. H., Lin, H. K., Scaglioni, P. P., Yung, T. M. and Pandolfi, P. P. (2006). The mechanisms of PML-nuclear body formation. *Mol. Cell* **24**, 331-339.
- Song, J., Durrin, L. K., Wilkinson, T. A., Krontiris, T. G. and Chen, Y. (2004). Identification of a SUMO-binding motif that recognizes SUMO-modified proteins. *Proc. Natl. Acad. Sci. USA* **101**, 14373-14378.
- Staudt, T., Lang, M., Medda, R., Engelhardt, J. and Hell, S. W. (2007). 2,2'-Thiodiethanol: a new water soluble mounting medium for high resolution optical microscopy. *Microsc. Res. Tech.* **70**, 1-9.
- Sternsdorf, T., Jensen, K. and Will, H. (1997). Evidence for covalent modification of the nuclear dot-associated proteins PML and Sp100 by PIC1/SUMO-1. *J. Cell Biol.* **139**, 1621-1634.
- Sternsdorf, T., Jensen, K., Reich, B. and Will, H. (1999). The nuclear dot protein sp100, characterization of domains necessary for dimerization, subcellular localization, and modification by small ubiquitin-like modifiers. *J. Biol. Chem.* **274**, 12555-12566.
- Takahashi, Y., Lallemand-Breitenbach, V., Zhu, J. and de The, H. (2004). PML nuclear bodies and apoptosis. *Oncogene* **23**, 2819-2824.
- Tatham, M. H., Geoffroy, M. C., Shen, L., Plechanovova, A., Hattersley, N., Jaffray, E. G., Palvimo, J. J. and Hay, R. T. (2008). RNF4 is a poly-SUMO-specific E3 ubiquitin ligase required for arsenic-induced PML degradation. *Nat. Cell Biol.* **10**, 538-546.
- Uchimura, Y., Ichimura, T., Uwada, J., Tachibana, T., Sugahara, S., Nakao, M. and Saitoh, H. (2006). Involvement of SUMO modification in MBD1- and MCAF1-mediated heterochromatin formation. *J. Biol. Chem.* **281**, 23180-23190.
- Weidtkamp-Peters, S., Lenser, T., Negorev, D., Gerstner, N., Hofmann, T. G., Schwantitz, G., Hoischen, C., Maul, G., Dittrich, P. and Hemmerich, P. (2008). Dynamics of component exchange at PML nuclear bodies. *J. Cell Sci.* **121**, 2731-2743.
- Weidtkamp-Peters, S., Weisshart, K., Schmiedeberg, L. and Hemmerich, P. (2009). Fluorescence correlation spectroscopy to assess the mobility of nuclear proteins. *Methods Mol. Biol.* **464**, 321-341.
- Weis, K., Rambaud, S., Lavau, C., Jansen, J., Carvalho, T., Carmo-Fonseca, M., Lamond, A. and Dejean, A. (1994). Retinoic acid regulates aberrant nuclear localization of PML-RAR alpha in acute promyelocytic leukemia cells. *Cell* **76**, 345-356.
- Yeager, T. R., Neumann, A. A., Englezou, A., Huschtscha, L. I., Noble, J. R. and Reddel, R. R. (1999). Telomerase-negative immortalized human cells contain a novel type of promyelocytic leukemia (PML) body. *Cancer Res.* **59**, 4175-4179.
- Zhong, S., Muller, S., Ronchetti, S., Freemont, P. S., Dejean, A. and Pandolfi, P. P. (2000). Role of SUMO-1-modified PML in nuclear body formation. *Blood* **95**, 2748-2752.

Supplementary Material

On the three-dimensional organization of promyelocytic leukemia nuclear bodies

Marion Lang, Thibaud Jegou, Inn Chung, Karsten Richter, Sandra Münch, Anikó Udvarhelyi, Christoph Cremer, Peter Hemmerich, Johann Engelhardt, Stefan W. Hell and Karsten Rippe

Supplementary Figure Legends

Fig. S1. CLSM overview images in HeLa and U2OS cells. Immunostaining was performed as described in the main text. The DNA was counterstained with DAPI. (A) PML and Sp100. (B) PML and SUMO-1.

Fig. S2. Imaging of PML protein by 4Pi microscopy with 1- and 2-photon excitation. Scale bars are 0.5 μm . Additional 1-photon 4Pi microscopy images of PML protein immunostaining in U2OS (A) and HeLa (B) cells are presented (see also Fig. 1 A, B). (C) 2-photon 4Pi microscopy images. (D) In control experiments it was confirmed that imaging the fluorescence signal from mRFP1-PML-III in transiently transfected U2OS (left) or HeLa cells (right) yielded the same PML-NB structure as immunostaining. The mRFP1-PML-III vector was derived from a previously made GFP construct (Weidtkamp-Peters *et al.*, 2008). (E) Comparison of raw and processed images obtained with 4Pi microscopy of type C for 2-photon excitation and 1-photon excitation. The raw data display the axially shifted side maxima, which are characteristic for 4Pi microscopy. In the case of appropriately low side maxima these can be easily removed by image processing, and the resulting images for 2-photon as well as for 1-photon excitation are depicted. While 4Pi microscopy with 2-photon excitation yields lower side maxima, 1-photon excitation gives a better signal-to-noise ratio. (F) Optical sections through a PML-NB (PML immunostaining) obtained with 1-photon excitation after removal of the side lobes.

Fig. S3. Analysis of PML protein density variations in PML-NBs. Scale bars are 0.5 μm . (A) Conventional CLSM images of small PML-NBs show that the spherical shell like organization of PML protein can not be resolved. Only for large PML-NBs ($> 1 \mu\text{m}$) as in the fourth image in panel A it can be seen in the xy -section of the CLSM images that the PML protein density is reduced in the interior. In general the optical resolution in the xz -plane is not sufficient to reveal the spherical shell structure of PML-NBs. (B-E) 4Pi xz -scans of PML-NBs. (B) 4Pi raw data of PML protein stained with an Alexa 568-labeled secondary antibody. The pixel intensity distribution clearly shows that the local variations exceed the shot noise of the measurement. For example the region indicated by a green box has 42 ± 7 photons on an average while in the blue box it is 67 ± 8 photons. (C) 4Pi images of Alexa 568 antibody staining of PML protein. (D) mRFP1-PML-III label. (E) GFP-PML-III label.

Fig. S4. Ultrastructure analysis by electron microscopy of PML-NBs in U2OS cells. PML-NBs were identified by correlative fluorescence and electron microscopy. Scale bar 1 μm . (A) Cross section through an irregularly shaped PML-NB. Similar to the two PML-bodies of Fig. 1 D, the extent of the body is defined by its shell. Also, dense granules of the embedding nucleoplasm are missing in the core of the body. (B) Enlarged view: Note the two-layered appearance of the shell (pair of arrows). (C, D) Two series of four consecutive 70 nm sections through two PML-bodies. The series in panel C represents an entire half-sphere of the body and demonstrates its spherical shape. Both PML-NBs are of the type with a dense core. The core appears separated from the layered shell (s. arrows). However, layered material can also occupy the core, as it can be seen in the third section of the lower series indicated with an arrow in panel D.

Fig. S5. Two-color 4Pi microscopy images of Sp100 and SUMO protein in U2OS cells. The cells were stained with an Alexa 568- (Sp100) and Atto 647-labeled (SUMO)

secondary antibody. Scale bars are 0.5 μm . The SUMO staining was carried out with a SUMO-1 antibody from mouse (Santa Cruz, D-11) that bound also to SUMO-2/3 (data not shown) as opposed to the staining with a SUMO-1 antibody from rabbit (Santa Cruz, FL-101) that was used for the immunostaining presented in Figure 4 A. The putative SUMO-1/2/3 signal shows some co-localization with Sp100 in the outer shell and is additionally found in the interior of the PML-NB. This is also apparent from the intensity profiles in the bottom row along the indicated lines. As in the case of the PML/SUMO-2/3 double staining presented in Fig. 4 B (merge 2) the SUMO signal was weak for a minority of PML-NBs as represented by merge 3.

Fig. S6. 4Pi microscopy images of PML-NB complexes with telomere repeats (APBs) in U2OS cells. Telomere repeats (green) were stained by FISH with a Cy3-labeled (CCCTAA)₃ peptide nucleic acid probe as described previously (Jegou *et al.*, 2009). PML bodies were visualized by immunostaining of PML protein (red) using an Alexa 647-coupled secondary antibody. Scale bars are 0.5 μm . (A) CLSM overview image of PML and telomere repeats. The cell shown had three APBs that are marked by the white arrows. (B) Two-color 4Pi microscopy of APBs. The first three images show PML (red), telomere repeat (green) and the corresponding merged image (merge 1). Then the merged images of PML and telomere repeats of two additional APBs are depicted (merge 2 and 3). Below the images intensity profiles taken along the lines indicated by numbers are plotted. They show that telomere repeats were located in the interior of APBs. (C) 3D image reconstructions from 4Pi microscopy images of APBs. The telomere repeat sequences are strictly confined to the interior of PML-NBs and are surrounded by a clearly separated PML protein shell

Fig. S7. 4Pi microscopy images of PML-NBs complexes with HP1 β . PML protein in HeLa cells was immunostained using an Alexa 647-labeled secondary antibody (red), while HP1 β was visualized by transient transfection with an mRFP1-HP1 β construct (green) kindly provided by Katharina Müller (Müller *et al.*, 2009). (A) CLSM overview

images of PML and GFP-HP1 β . Three complexes of a PML-NB with HP1 β are indicated by arrows. The DNA was counterstained with DAPI. (B) In the panel the first three images show PML (red), mRFP1-HP1 β (green) and the corresponding merged image (merge 1). In addition, the merged images of PML and HP1 β of two other PML-NBs are depicted (merge 2 and 3). Below the images intensity profiles taken along the lines indicated by numbers are plotted. (C) 3D image reconstructions from 4Pi microscopy images. HP1 β was located in the PML-NB interior.

Fig. S8. PML body structure during mitosis. PML-NBs were immunostained with an Alexa 568-coupled secondary antibody while Sp100 or SUMO-1 proteins were visualized via an Alexa 633-coupled secondary antibody. (A) Conventional wide-field fluorescence microscopy images with a DAPI DNA-counterstaining showed a diffuse distribution of SUMO-1 or Sp100 (green) relative to PML protein (red). (B) The fine structure of PML bodies during mitosis was evaluated by 4Pi microscopy in U2OS and HeLa cells. The 4Pi images revealed that during mitosis the spherical shell organization of PML protein in PML-NBs breaks down into an amorphous aggregated conformation. Scale bars are 0.5 μ m.

Supplementary References

Jegou, T., Chung, I., Heuvelmann, G., Wachsmuth, M., Görisch, S. M., Greulich-Bode, K., Boukamp, P., Lichter, P. and Rippe, K. (2009). Dynamics of telomeres and promyelocytic leukemia nuclear bodies in a telomerase negative human cell line. *Molecular Biology of the Cell* **20**, 2070-2082.

Müller, K., Erdel, F., Caudron-Herger, M., Marth, C., Fodor, B. D., Richter, M., Scaranaro, M., Beoudoin, J., Wachsmuth, M. and Rippe, K. (2009). A multi-scale analysis of dynamics and interactions of heterochromatin protein 1 in the nucleus by fluorescence fluctuation microscopy. *Biophysical Journal*, in revision.

Weidtkamp-Peters, S., Lenser, T., Negorev, D., Gerstner, N., Hofmann, T. G., Schwanitz, G., Hoischen, C., Maul, G., Dittrich, P. and Hemmerich, P. (2008). Dynamics of component exchange at PML nuclear bodies. *J Cell Sci* **121**, 2731-43.

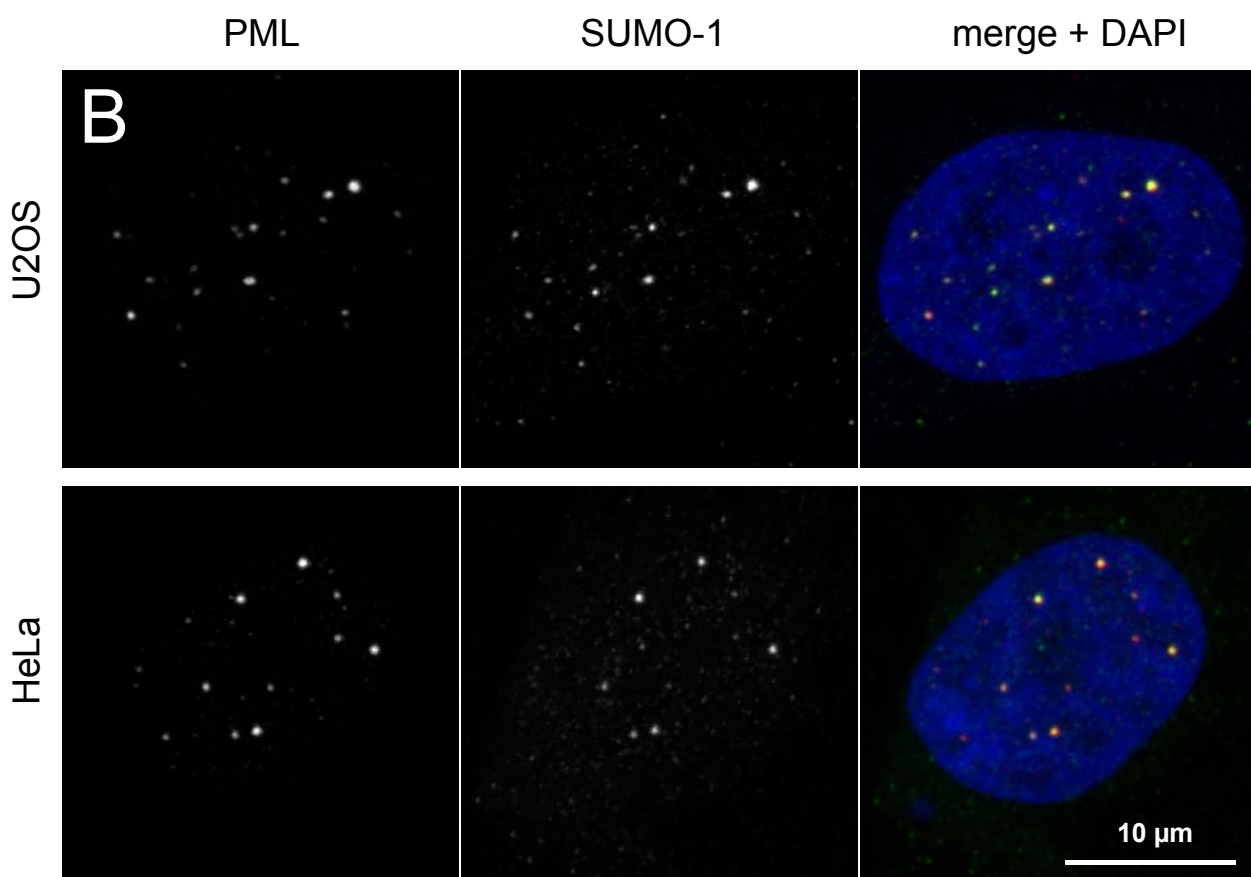
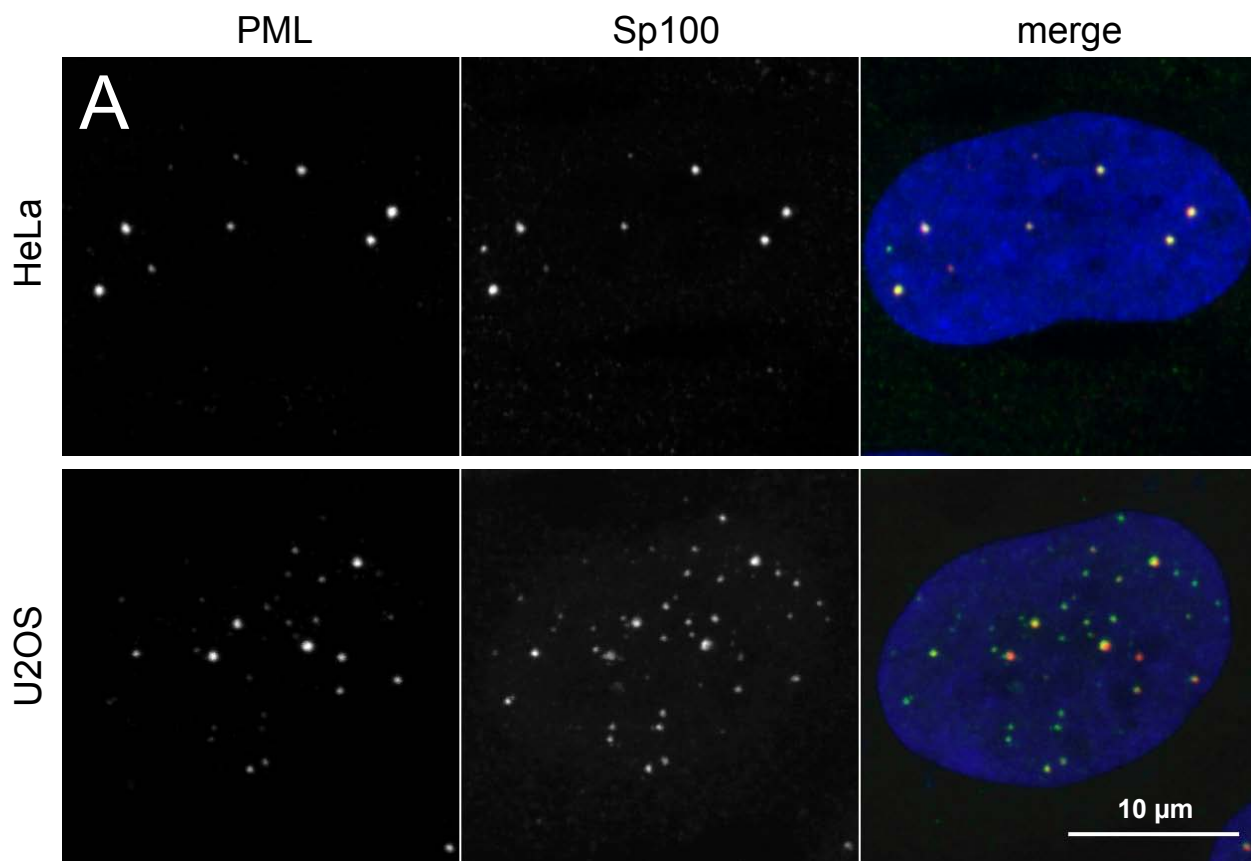


Fig. S1, Lang et al.

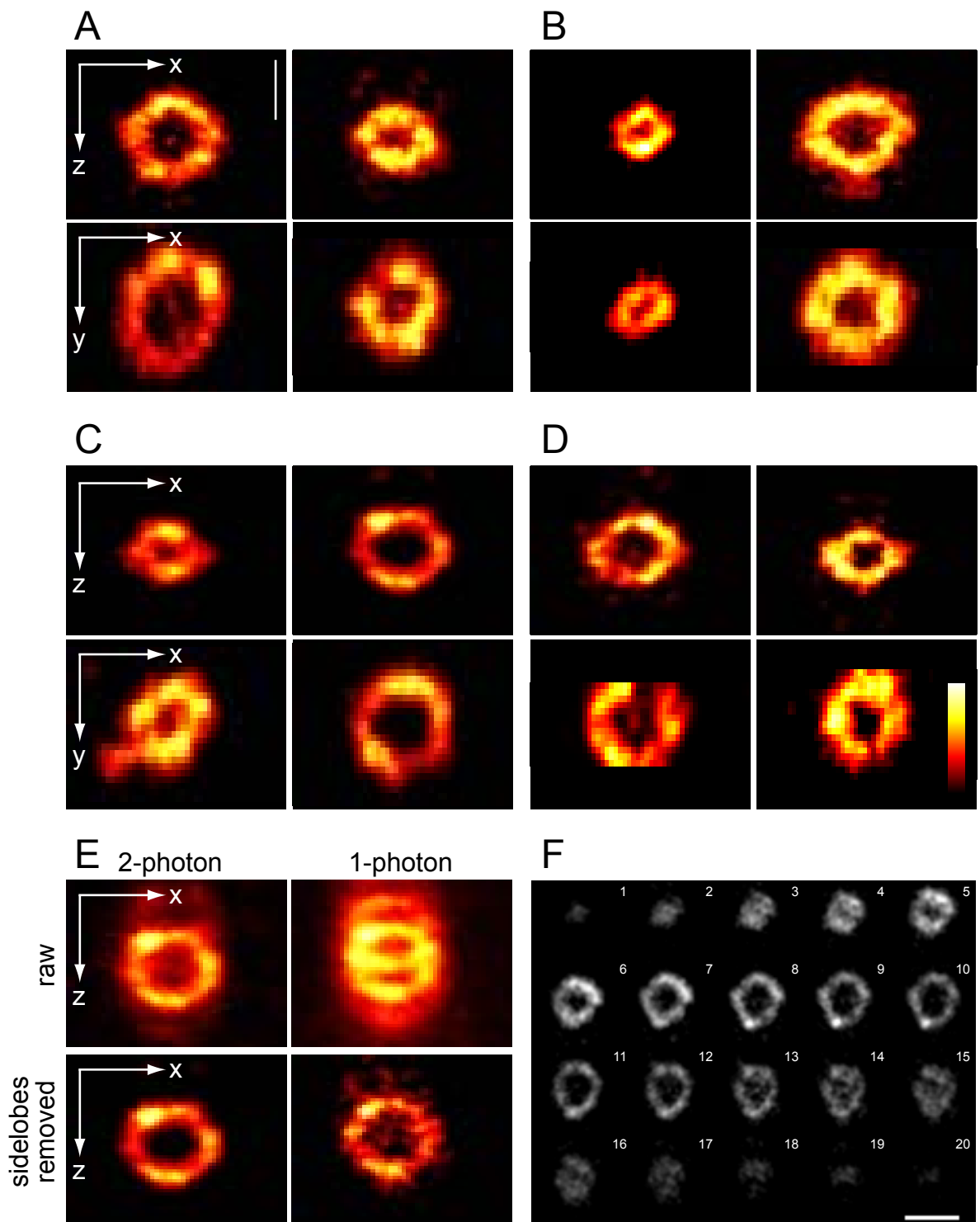


Fig. S2, Lang et al.

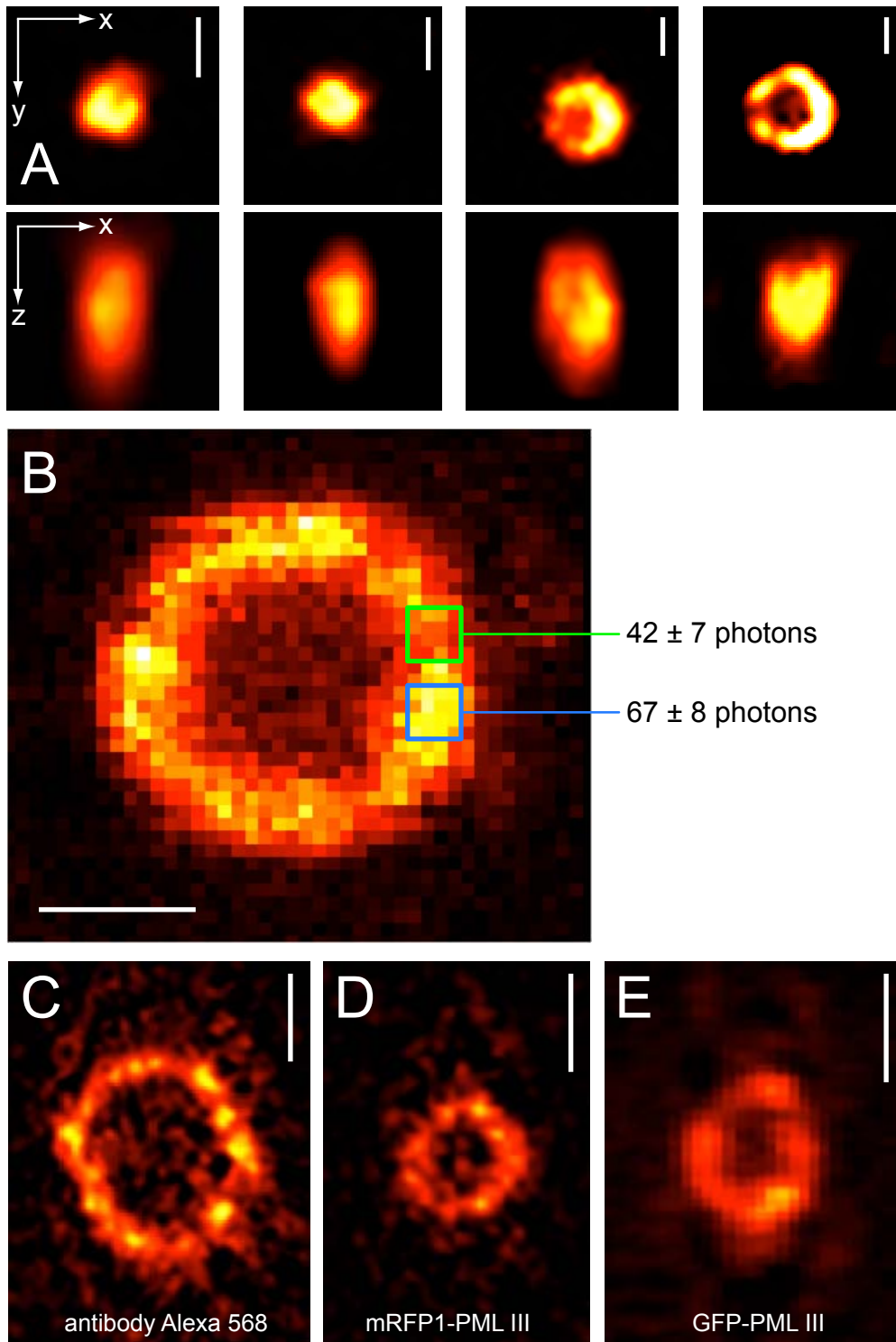


Fig. S3, Lang et al.

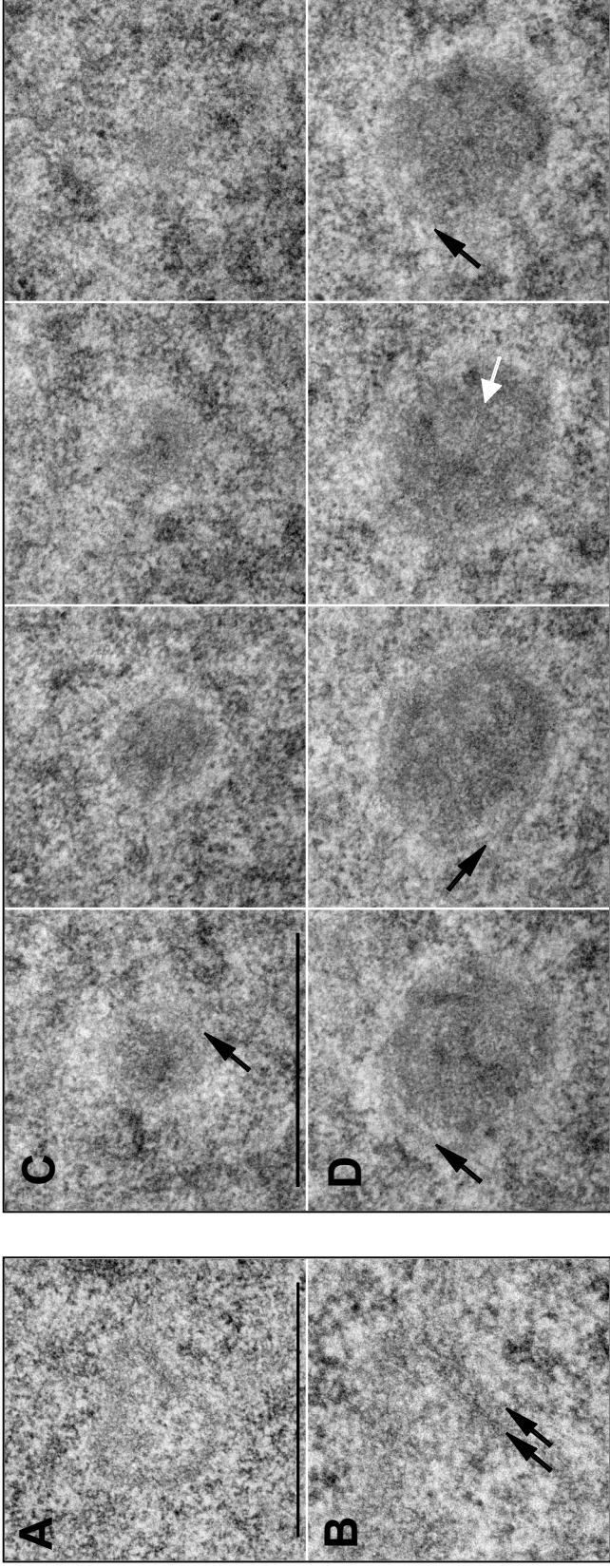


Fig. S4, Lang et al.

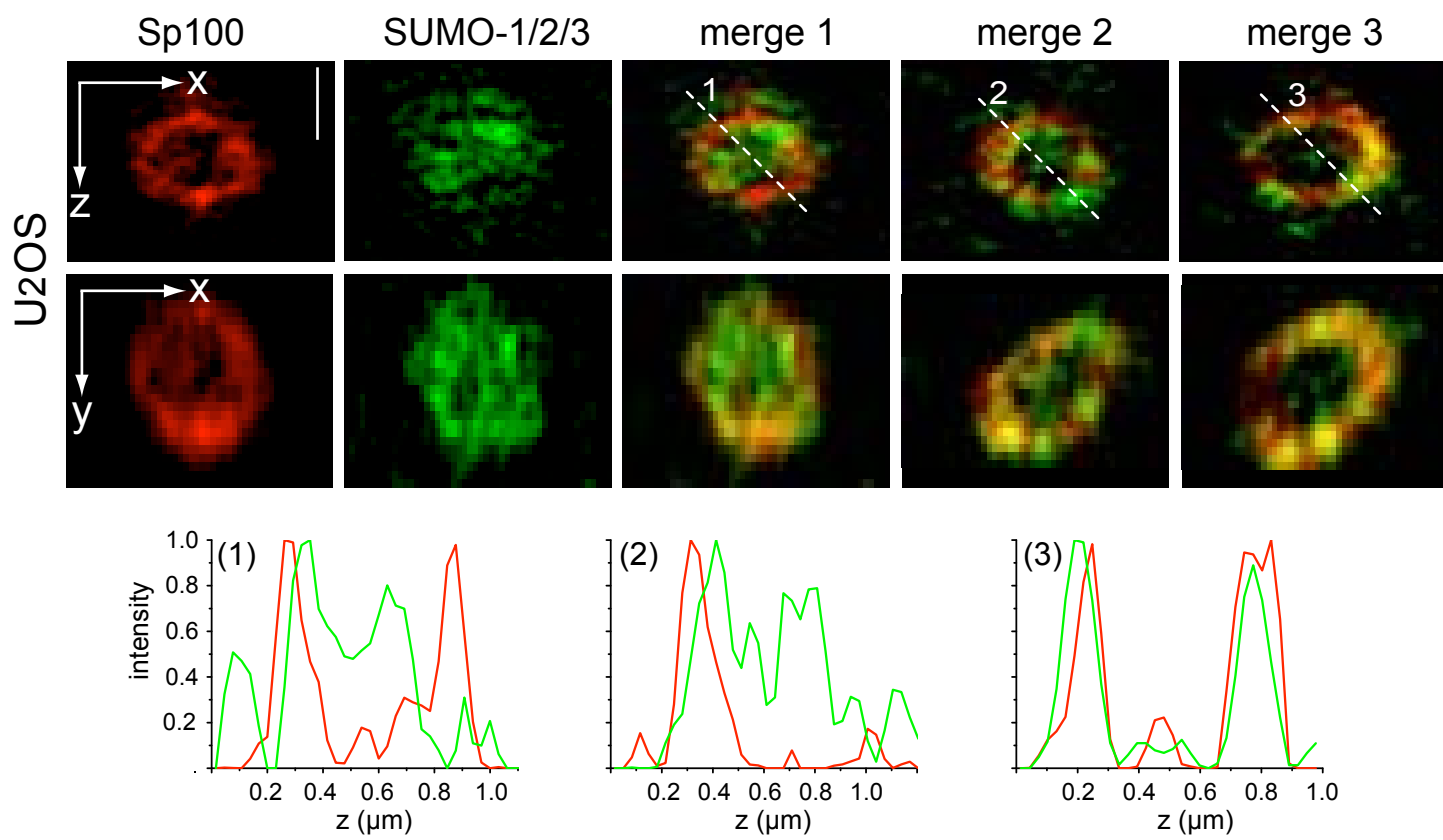


Fig. S5, Lang et al.

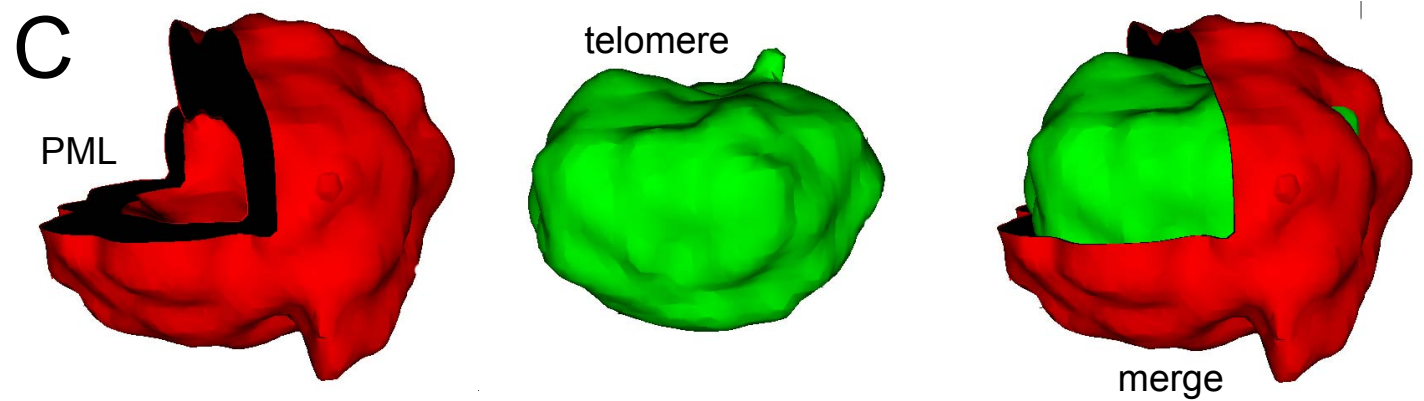
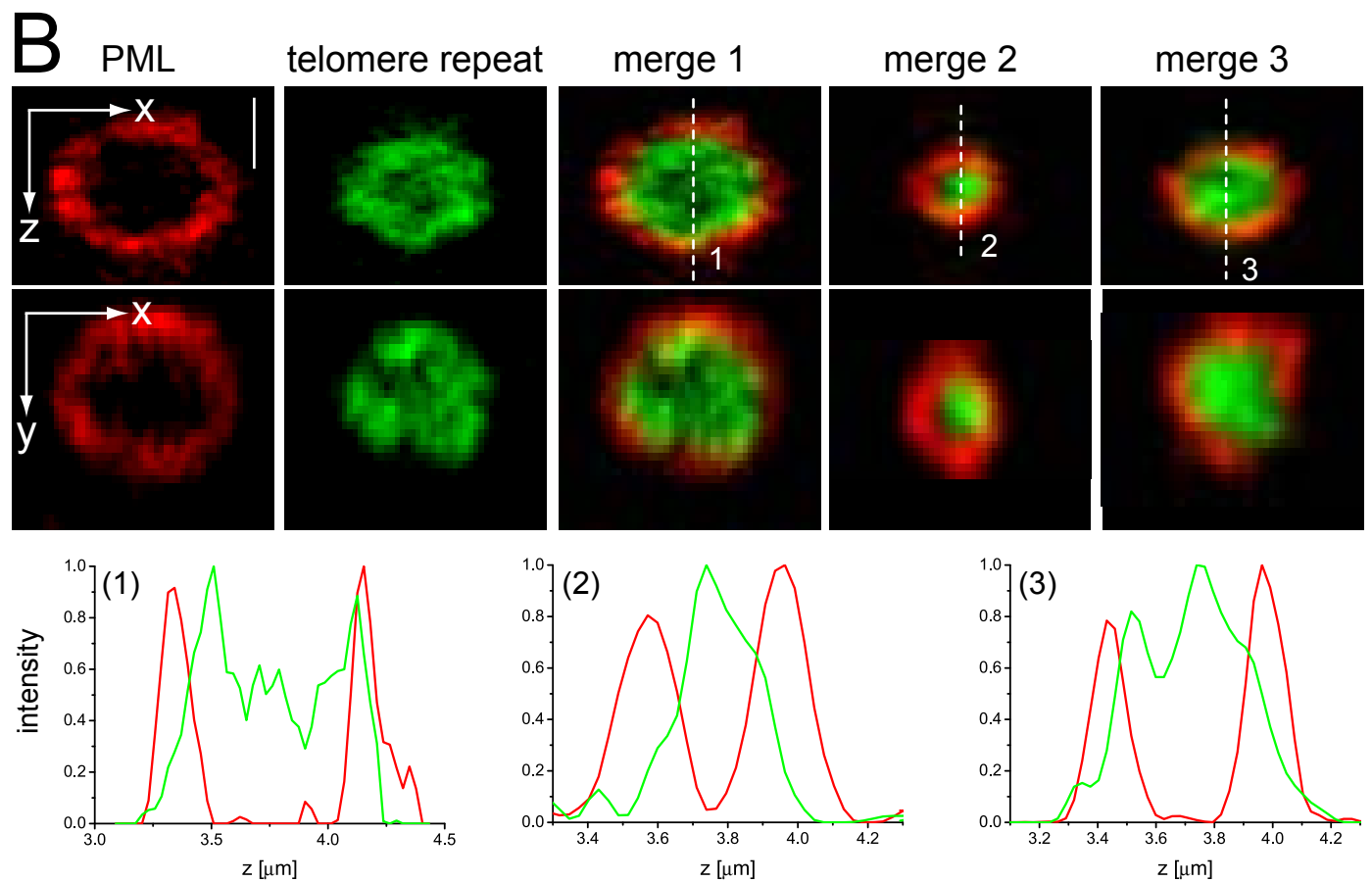
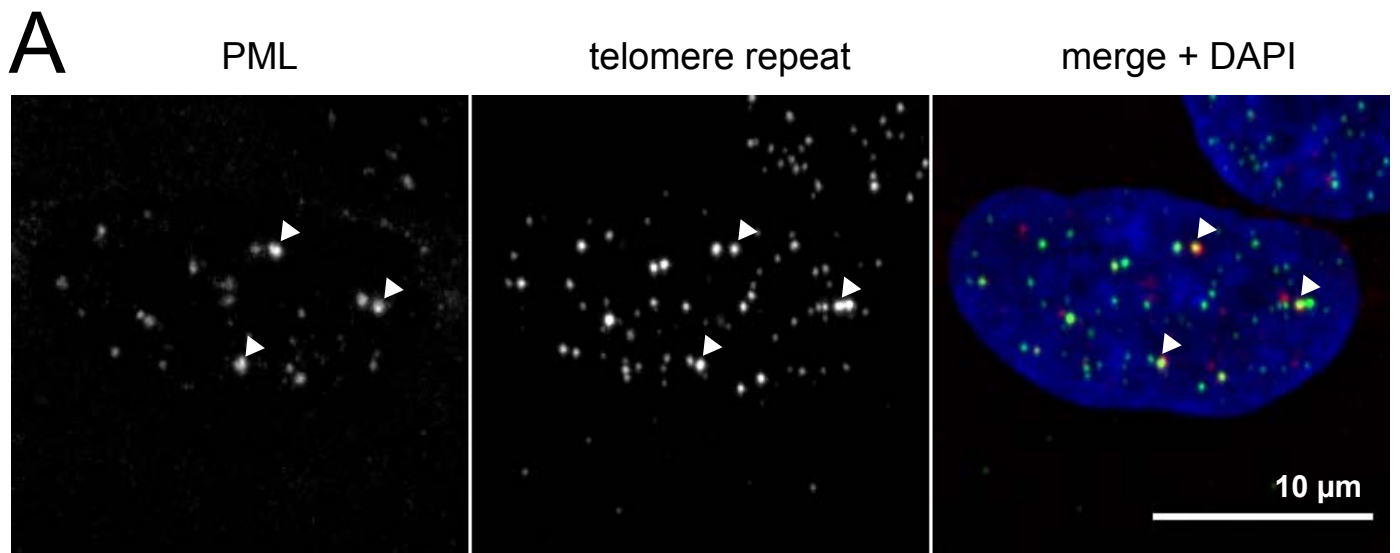


Fig. S6, Lang et al.

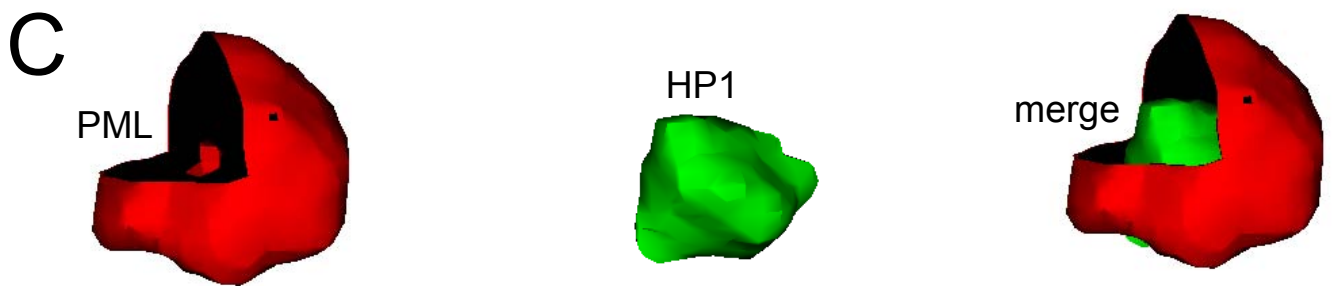
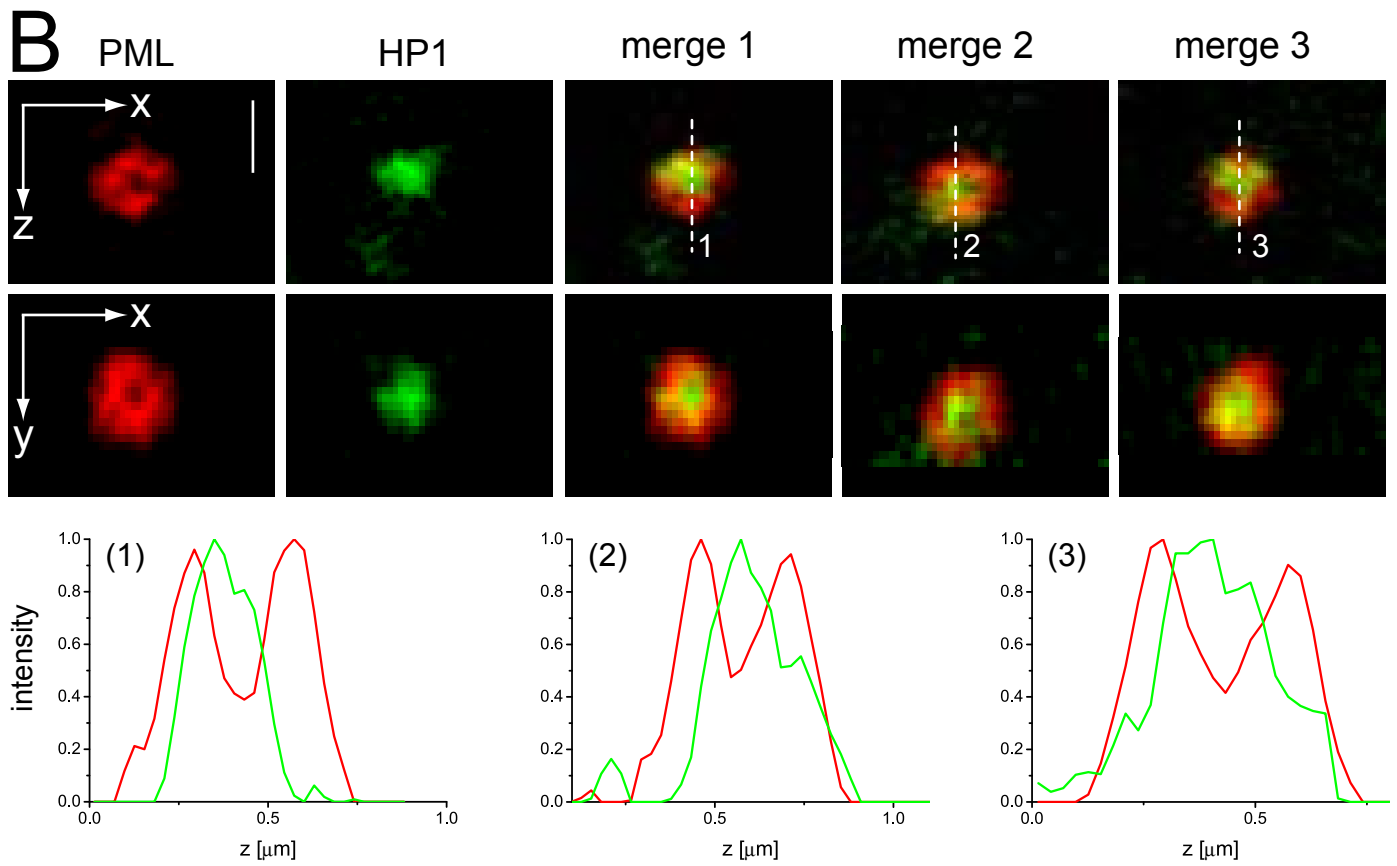
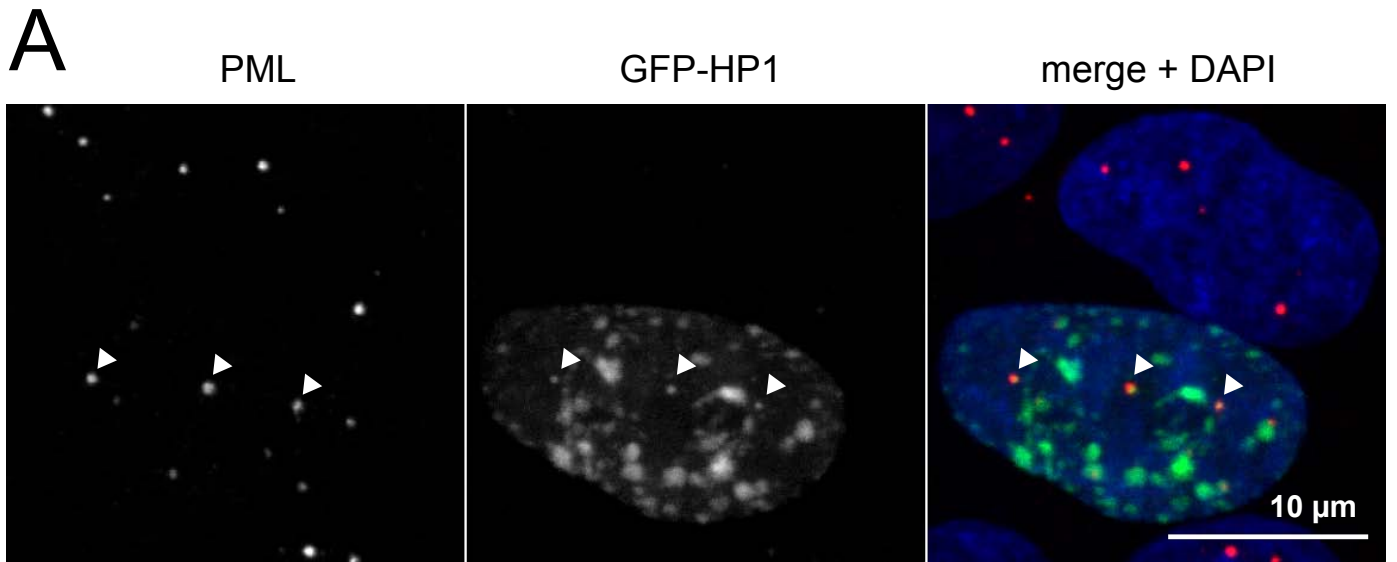


Fig. S7, Lang et al.

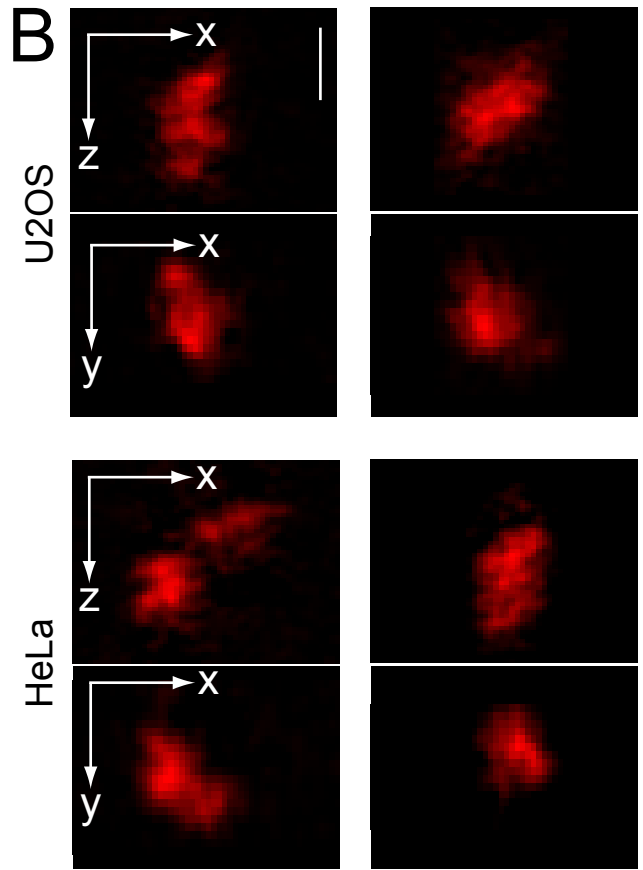
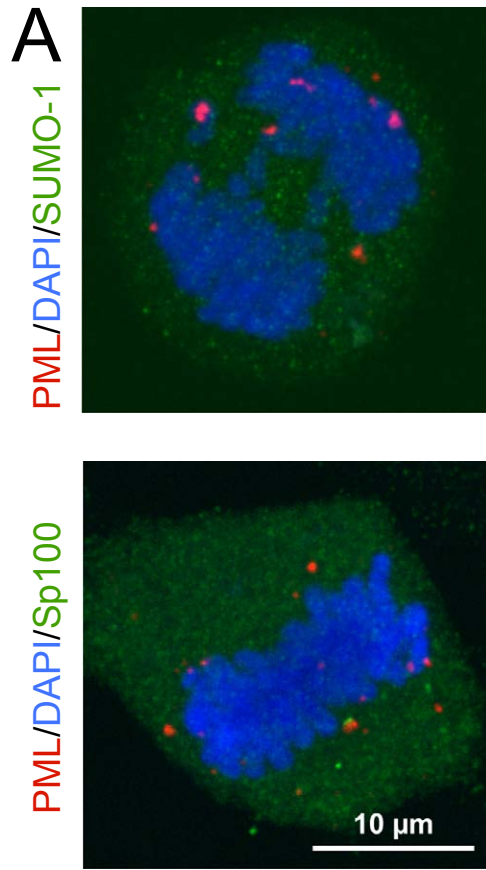


Fig. S8, Lang et al.